ENERGY LABORATORY LEVEL II ⑫ 85 MASSACHUSETTS INSTITUTE
AND OF TECHNOLOGY
MATERIALS PROCESSING CENTER

SINTERABLE POWDERS
FROM
LASER DRIVEN REACTIONS

BY

John S. Haggerty

W. Roger Cannon

July 1980

DTIC
SELECTED
MAY 28 1981
A

BUILDING NO. 12
MASSACHUSETTS INSTITUTE OF TECHNOLOGY
CAMBRIDGE, MASSACHUSETTS 02139

81 5 28 023

(6) SINTERABLE POWDERS FROM LASER DRIVEN REACTIONS.
THIRD ANNUAL REPORT

(9) Annual rept. no. 3, 1 Jul 79 - 30 Jun 80,

(10)
John S. Haggerty

W. Roger Cannon

Energy Laboratory

(11) Jul 80   (12) 113

(14) MIT-EL-81-003

Massachusetts Institute of Technology
Cambridge, Massachusetts 02139

Prepared for:

The U. S. Department of Defense

411006

The views and conclusions contained in this document are those
of the authors and should not be interpreted as necessarily
representing the official policies, either expressed or implied
of the Defense Advanced Research Agency or the U. S. Government.

REPORT DOCUMENTATION PAGE	READ INSTRUCTIONS BEFORE COMPLETING FORM

1. REPORT NUMBER	2. GOVT ACCESSION NO.	3. RECIPIENT'S CATALOG NUMBER
MIT-EL-81-003	AD-A099 433	

4. TITLE (and Subtitle)	5. TYPE OF REPORT & PERIOD COVERED
Sinterable Powders from Laser Driven Reactions	1 July 79 - 30 June 80 Third Annual Report
	6. PERFORMING ORG. REPORT NUMBER MIT-EL-81-003

7. AUTHOR(s)	8. CONTRACT OR GRANT NUMBER(s)
John S. Haggerty, W. Roger Cannon	N00014-77-C-0581

9. PERFORMING ORGANIZATION NAME AND ADDRESS	10. PROGRAM ELEMENT, PROJECT, TASK AREA & WORK UNIT NUMBERS
Massachusetts Institute of Technology Cambridge, Massachusetts 02139	NR 039-153/12-12-3-80

11. CONTROLLING OFFICE NAME AND ADDRESS	12. REPORT DATE
O. N. R. Department of the Navy 800 North Quincy Street, Arlington, VA 22217	December 1979
	13. NUMBER OF PAGES 103

14. MONITORING AGENCY NAME & ADDRESS(If different from Controlling Office)	15. SECURITY CLASS. (of this report)
	Unclassified
	15a. DECLASSIFICATION/DOWNGRADING SCHEDULE

16. DISTRIBUTION STATEMENT (of this Report)

Unrestricted

17. DISTRIBUTION STATEMENT (of the abstract entered in Block 20, if different from Report)

Unrestricted

18. SUPPLEMENTARY NOTES

19. KEY WORDS (Continue on reverse side if necessary and identify by block number)

Laser synthesis of powders	Laser heated gases
Laser driven reactions	Silicon carbide powder
Gas phase synthesis of powders	Ceramic powders
Silicon powder	
Silicon nitride powder	

20. ABSTRACT (Continue on reverse side if necessary and identify by block number)

Extremely fine, uniform ceramic powders have been synthesized from SiH_4, NH_3 and C_2H_4 gas phase reactants that are heated by absorbing optical energy emitted from a CO_2 laser. Resulting Si, Si_3N_4 and SiC powders have been characterized in terms of parameters which are important for densification processes. They are virtually ideal. The spherical particles typically have mean diameters from 120 to 1000 Å. The standard deviation is typically 25-45% and the diameter of the largest observed particle is

DD FORM 1473 EDITION OF 1 NOV 65 IS OBSOLETE
1 JAN 73
S/N 0102-014-6601

(approximately)

typically less than twice that of the smallest particle. Purities are extremely high. The laser heated process has been modeled in terms of fluid flow and heat transfer criteria. Many fundamental property measurements were made to provide data for these calculations. The process is extremely efficient, $\sim$ 95% of the SiH_4 is reacted in a single pass through the laser beam and approximately 2 kwhr. of energy are required per kilo of Si_3N_4.

The resulting powders have been processed into dense pieces using several shaping techniques. The Si powders were densified to precisely controlled levels designed to yield high density reaction bonded silicon nitride (RBSN). Nitriding knetics were rapid at low temperatures because of the small particle sizes. Characteristic dimensions of RBSN microstructures approximated the initial particle dimensions. Sintering experiments with pure Si_3N_4 powder gave indications that densification occurred on a local scale.

Accession For

NTIS GRA&I
DTIC TAB
Unannounced
Justification

By
Distribution/
Availability Codes

Dist	Avail and/or Special
A	

TABLE OF CONTENTS

LIST OF FIGURES

LIST OF TABLES

FORWARD

This research program involved several groups within M.I.T. which represented different technical disciplines. The novelty of these processes for using lasers to produce ideal powders has intrinsically required an interdisciplinary approach. The principal investigators, Drs. J. S. Haggerty and W. R. Cannon, are materials scientists associated with both the Energy Laboratory and The Department of Materials Science and Engineering, as is Dr. S. C. Danforth, who has worked on all aspects of this program. Dr. S. Mizuta and Mr. J. Flint are Research Associates. Mr. R. A. Marra, Ms. L. Schioler and Mr. H. Sawhill are graduate students and Research Assistants in the Department of Materials Science and Engineering. Ms. M. Gabriel and Mr. M. Schmaier are undergraduate students in the same department who have worked on the project under the Undergraduate Research Opportunities Program. Everyone's contributions are gratefully acknowledged.

I INTRODUCTION

Increasingly, because of their superior properties, ceramic materials are being considered for applications involving high stress levels. The important properties include hardness, high temperature strength, erosion, oxidation and corrosion resistance, low density and, for some uses, specific electrical and optical properties. Their use in many of these applications can only be considered if their reliability is improved. As brittle materials, they fail catastrophically when a strength limiting defect becomes unstable in a stress field and propagates. In most cases, failure of an individual ceramic element would halt or dammage the entire system in which it was used. The wide distribution of strengths observed with ceramic materials forces engineers to design so conservatively that ceramics lose their intrinsic advantages relative to conventional materials.

Strength limiting defects are usually attributable to some specific event in the parts processing history extending from powder synthesis through all the handling steps to the final consolidation into a densified part. There are many causes for strength limiting defects and their elimination continues to be the subject of processing research and component development programs. At M.I.T., we are approaching this problem from a new perspective[1] which requires that constituent powders satisfy rigid criteria. With the correct powders and handling procedures, it is possible to cause the individual particles to arrange in a close packed structure as shown in Figure 1. Bodies having this unusual internal structure will exhibit low, uniform shrinkage to theoretical density with low firing temperatures and short times. Short, low temperature densification cycles should virtually eliminate grain growth. Also, the characteristic size of remaining flaws should be approximately that of the particles since individual vacancies are the largest defect.

This research program has investigated laser means of producing powders with the following ideal characteristics: (1) the powder must have a small particle size, typically less than 0.5 μm; (2) the particles must be free of agglomerates; (3) the particle diameters must have a narrow range of sizes; (4) the morphology of the particles must be equiaxed, tending toward spherical shapes; (5) the powders must have highly controlled purity with respect to contaminants and multiple polymorphic phases. Either with or

1
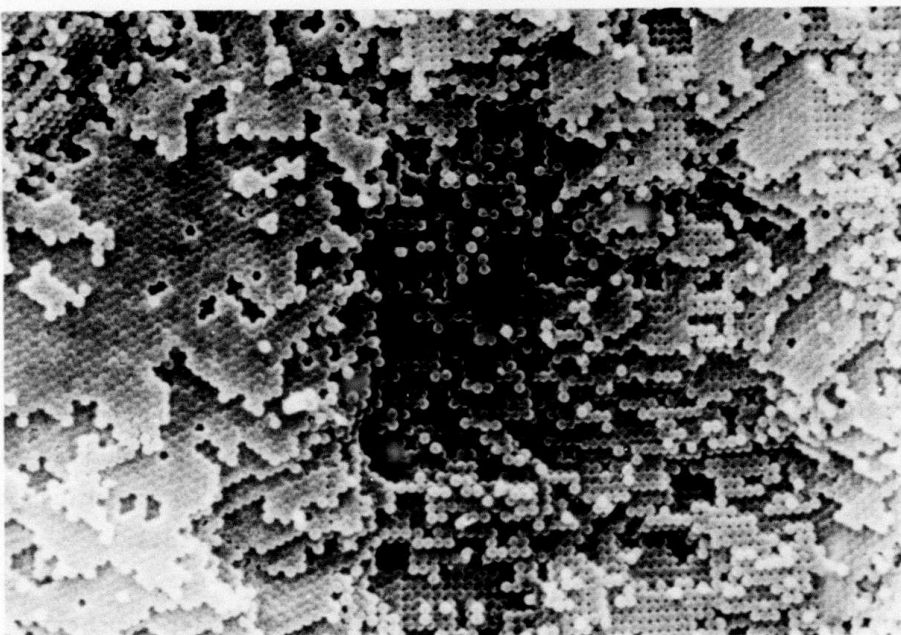
Figure 1. Ordered packing of monodispersed 0.2 μm diameter SiO_2 spheres.

without the ordered structures shown in Figure 1, a powder exhibiting these ideal characteristics should be sinterable to theoretical density without resorting to pressure or additives and should permit the final grain structure to be highly controllable.

Because existing powder synthesis techniques cannot produce powders with these requisite characteristics, we have undertaken to determine whether laser heated processes could. We investigated a selective comminution process in the first year[2]. Since then, we have concentrated on a laser heated gas phase synthesis process, once it was demonstrated we could achieve the process conditions which result in uniform nucleation and growth histories[2,3]. This phase of the program has emphasized synthesis of Si and Si_3N_4 powders. Preliminary synthesis experiments have been made with SiC. The Si powders are used for the reaction bonding process in which densification and conversion to Si_3N_4 occur simultaneously. We have had two specific objectives. Our initial and primary objective has been to develop a process for producing ceramic powders with characteristics that will

permit a better understanding of the interactions between powder
characteristics, densification processes, and the properties of ceramic
bodies. Secondly, since very specific powder characteristics are required
to satisfy this objective, we have concentrated on developing an analytical
description of the synthesis process.

Several commercial processes are being used to synthesize Si_3N_4 and
SiC powders. Typically they involve DC arcs, conventional vapor phase
reactions in heated tube furnaces and nitriding or carbiding of silicon
metal. The nitriding of silicon metal typically leaves a silicon core
within the silicon nitride particle. Furthermore, because the process is
done in the solid state, particles must be separated by grinding, which does
not result in a narrow size distributed, non-agglomerated, phase pure
powder. The vapor phase methods (furnace heated vapor and arc plasma
techniques) yield finer and more uniform powders than the nitriding of solid
silicon, but these techniques have less than ideal thermal profiles in their
reaction zones which cause a distribution of nucleation and growth times and
the formation of agglomerates. Despite these specific process deficiencies,
synthesis from dilute gas phase reactants is one of the most promising
routes for producing powders having these specific ideal characteristics.

The laser driven gas phase reaction process investigated in this
program offers many advantages. It is a clean process because no
potentially contaminating surfaces are heated. The reaction zone is
precisely defined, consisting of the volume enclosed by the reactant gas
stream and resulting particles and the laser beam. The ability to maintain
steep temperature gradients in the effective thermal environment, and thus a
well defined reaction zone, should allow precise control of the nucleation
rate, the growth rate and exposure times, permitting the nucleation and
growth of very fine uniformly sized particles. The available power levels,
the stability of the delivered power, cost, reliability and conversion
efficiency all suggest the use of a CO_2 laser source provided that gases are
identified which are optically absorbing at emitted wavelengths.

To develop an understanding of the interrelationships between powder
characteristics and the synthesis process, it is necessary to be able to
describe heating rates, nucleation and growth rates and the distributions of
temperature and mass flow throughout the "reaction zone". We have studied

3

the effect of several process variables on powder characteristics[2,3]. These include beam intensity, gas composition (stoichiometry and dilution), gas pressure, and gas velocity. The effect of these process parameters has been correlated with both powder characteristics and process characteristics, e.g. emitted spectra, temperature, and percent conversion.

Two fundamentally different types of reactions have been investigated. Most of our work has been carried out under laser intensity and gas pressure conditions where many collisions occur between the gas molecules during the period that they are heated. These reactions probably proceed as normal thermal reactions. In this case, the principal advantages of the laser heat source are process control and possibly unique reaction paths because of high heating rates and resonance effects between the coherent light and the molecules. The second type of reaction is uniquely possible with laser heating. In this case, molecules absorb sufficient energy to dissociate before colliding with other molecules.

The uses of this synthesis technique as an experimental tool has tremendous potential, and its eventual use as a production tool appears increasingly probable. It is now apparent that it can be applied to elements, oxides, carbides, and nitrides. With slightly different process conditions, it can be used to deposit thin films rather than producing powders.

II SUMMARY OF PREVIOUS WORK

A. Objectives and Approaches

The broad objective of this program has been to find laser means of producing powders which exhibit the characteristics stated in the Introduction and then to demonstrate that superior properties and/or processing characteristics result from using them. Our specific objectives have changed during the course of the program as various important issues were resolved favorably. During the first two years[2,3], we conducted research to determine the basic feasibility of the laser comminution and laser heated gas phase synthesis processes. Resulting powders have been fully characterized throughout the program. In year 3, we concentrated on developing descriptions of both the laser heated process for synthesizing the three materials of interest, as well as the interaction between process variables and powder characteristics. We also began processing the resulting powders into shapes. In year 4, we will concentrate on processing the resulting powders, and evaluating the properties of the ceramic pieces to study the interaction between process variables and properties. Based on the success of the synthesis process, we will begin to consider issues relating to scaling the process to production levels.

B. Process Descriptions

1. Gas Phase Synthesis Process

The powder synthesis process employs an optical energy source to transfer the energy required to initiate and sustain a chemical reaction in the gas phase. In this process, the gas molecules are "self-heated" throughout the gas volume, a process which is distinct from conventional ones where heat is transmitted from a source to the gas molecules by a combination of conduction, convection and radiative processes. The advantages of this means of heating are freedom from contamination, absence of surfaces that act as heterogeneous nucleation sites, and unusually uniform and precise process control. These attributes should permit the synthesis of powders with characteristics that are ideal for making ceramic bodies.

A laser, rather than other possible optical heat sources, has been used because of the narrow spectral width of emitted light and the brightness of

this type of light source. The coherency of the light was not considered an important feature for this process. Coupling between the source and absorber requires virtual coincidence between the emission and the absorption lines. If this matching occurs, the optical-to-thermal efficiency can be extremely high and the overall process efficiency is essentially that of the laser. This efficiency is much higher than is possible with broad band light sources because only small fractions of their light are absorbed by the gases. With CO_2 lasers, as have been used in this program, the overall process efficiency matches or exceeds that of other conventional heat sources, e.g. various types of plasmas, torches or heated tubes. In addition to the high efficiency, the use of laser energy sources makes possible unique reaction paths which may produce powders with unusual characteristics.

Two basic ranges of laser intensity and exposure time have been investigated. Most of the synthesizing research has been carried out in conditions typical of the normal or thermal domain. We have also investigated the process under conditions anticipated to produce multiphoton, unimolecular reactions. All of the powders discussed in this report were produced under the lower intensity, high gas pressures where normal thermal reactions occur.

The laser beam enters the reaction chamber, Figure 2, through a KCl window and is arrested with a water cooled copper block. Power intensities range from 270-1020 watts/cm^2 for the unfocused beam, and up to 10^5 watts/cm^2 near the focal point of a 13 cm lens. The reactant gases (SiH_4 for Si, NH_3-SiH_4 for Si_3N_4, and C_2H_4-SiH_4 for SiC) enter the cell orthogonal to the laser beam through a 1.5 mm stainless steel nozzle 2-3 mm below the laser beam. A coaxial argon stream is used to suppress the expansion of the product stream with entrained particles, so these particles can be collected in a microfiber filter. Argon gas is directed across the KCl window to prevent powder collection there and possible breakage. The reactant gases employed are electronic grade SiH_4, NH_3, and C_2H_4. Prepurified argon is used as the inert buffer gas. The Ar gas train includes a Ti oxygen getter which typically achieves < 1 ppm O_2. Reaction cell pressures, ranging from 0.08 to 1.0 atm, are maintained by a throttling valve in series between the filter and the vacuum pump.
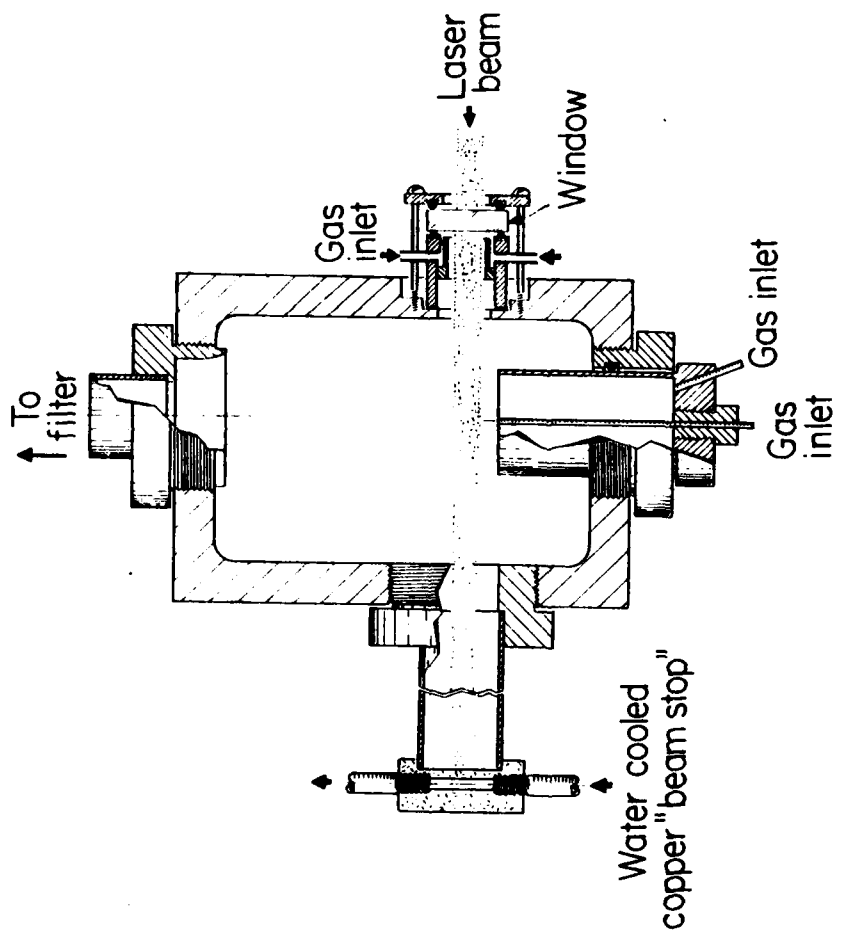
Figure 2. Schematic of powder synthesis cell.

TABLE I

Reference Processing Conditions for Synthesis of Si, Si_3N_4, and SiC Powder

Powder Type	Si	Si_3N_4	SiC
Cell Pressure (atm)	0.2	0.2	0.2
SiH_4 Flow Rate (cc/min)	11	11	11
NH_3 Flow Rate (cc/min)	0	110	0
C_2H_4 Flow Rate (cc/min)	0	0	9
Argon Flow Rate (cc/min) (to window)	600	600	600
Argon Flow Rate (cc/min) (to annulus)	400	400	400
Laser Intensity (W/cm^2)	760	760	760

Table I gives the set of reference process variables used for Si, Si_3N_4, and SiC production. These conditions were viewed as a benchmark or reference point from which systematic variations were made. Typically 2-5 watts are absorbed by the gas steam for NH_3/SiH_4 and 30 watts for SiH_4 or SiH_4/C_2H_4. The gas stream is kept optically thin to maximize the uniformity of the thermal histories for all gas elements.

The powders produced in the reaction zone are carried into the collection filter by the product and argon gases. The process typically produces 1 to 10 grams of powder per hour. Up to 10 grams can be collected before the filter fills and it is no longer possible to maintain a constant cell pressure. With recent modifications, virtually all of the powder is transported to the filter. Based on mass balance, the laser induced reaction typically converts 85 - 100% of the reactants to products. The collected powders are sealed in the microfiber filter under a positive argon pressure. This filter assembly is then transferred into a glove box through

8

a vacuum antechamber. All post-production handling is performed in a nitrogen environment maintained at less than 10 ppm each of O_2 and H_2O. None of these powders oxidize pyrophorically on exposure to air.

The results of this research program demonstrate that the laser heated synthesis process yields powders having virtually all of the desired characteristics. The resulting particles are small ($\leq$ 1000 Å), uniform in size, spherical, and pure. The particles appear to be attached to one another in chain-like agglomerations, however, direct examination by TEM usually shows no neck formation between Si_3N_4 and SiC particles. We anticipate that they can be dispersed. Besides producing powders with ideal characteristics, the laser heated synthesis process is extremely efficient. Approximately 95% of SiH_4 is converted to Si_3N_4 powder in a single pass through the laser beam. Also, Si, Si_3N_4 and SiC powders can be produced from these reactants with as little as 2 kWhr of energy per kilogram of powder. It is likely that this process can produce both a superior and lower cost powder than conventional gas phase or solid phase synthesis processes.

Much of our effort has focused on developing an analytical description of the laser heated synthesis process. To develop a model, many fundamental property measurements were required, such as detailed absorptivity measurements for reactant gases as a function of pressure and emitted wavelength. Emissions from the reaction have been studied to identify reaction species and to estimate the reaction temperature. Computer analyses of the gas flow were used to predict gas stream dimensions and velocities. Combined with direct observations of both the reaction positions relative to the laser beam and the reaction temperatures, these analyses and characterizations have been used to describe the time-temperature history of the reactant gases throughout the course of the reaction.

Most process variables were manipulated to determine their effect on particle characteristics. The variables which have a direct effect on the nucleation and growth kinetics include reaction temperature, heating rate, partial pressure of reactants, total pressure and dilution by inert gases. Most of these variables were manipulated to demonstrate their empirical effect on Si_3N_4 powder characteristics[3]. Prior to this report, only preliminary experiments had been done with Si.

9

We examined the following powder characteristics: size, size
distribution, shape, stoichiometry, chemical impurities, and crystallinity.
Process variables which were changed are laser intensity, cell pressures,
gas velocities and, to a lesser extent, gas mixture. Of the characteristics
and process variables examined, only particle size and stoichiometry were
influenced by laser intensity and gas pressure. No other variable had any
significant effect on any other characteristics within the range of
conditions examined.

    a. Effects of Process Variables

       i. Laser Intensity

Increased laser intensity caused the Si_3N_4 particle size to decrease
and caused the Si/N ratio of Si_3N_4 particles to approach the stoichiometric
composition.

We have shown that virtually all of the silane gas is consumed during
particle growth, thus the particle size is limited by impingement of
overlapping volumes of depleted reactant gas. The final particle size is
therefore controlled by the number of embryos which reach supercritical
dimensions and grow until the depleted volumes impinge upon one another.
The homogeneous nucleation rate is very small until either the degree of
supersaturation approaches a critical value or, if kinetically limited, a
critical temperature is reached. The rate changes many orders of magnitude
with small changes beyond either of these critical values. The narrow
particle size distribution indicates that there was no appreciable
nucleation during the time period between the appearance of the initial
nuclei and cessation of growth with impingement. This can occur for two
reasons. The growth process itself may effectively terminate the nucleation
process by, for instance, reducing the supersaturation level below the
critical level. Or, at the critical supersaturation level, where nucleation
rates first become appreciable, the growth rates may be extremely fast. In
this case, the reaction effectively goes to completion and terminates with
the appearance of the first nuclei.

The decrease in Si_3N_4 particle size with increased laser intensity
results from forcing the spontaneous reaction temperature to higher levels
with the higher heating rates and correspondingly higher degrees of
supersaturation. Heating rates at the reaction temperature ranged from 10^6
to 10^8 °C/sec for laser intensities ranging from 760 to 10^5 watts/cm^2. The

10

particle size is reduced because the nucleation rate is larger at higher temperatures, and it increases proportionally faster than the growth rate. This is the same conclusion reached for TiO_2 powders produced from $TiCl_4-O_2$ mixtures.[4]

The general defficiency of nitrogen in resulting Si_3N_4 particles could be caused by either slow reaction kinetics involving nitrogen-bearing species or by preferential vaporization of nitrogen from hot particles. These results indicate that higher temperatures permit achievement of stoichiometric compositions for kinetic reasons. The effect of increased kinetic rates is self-assisting because the increasingly rapid exothermic reactions involved in the growth process drive the particle temperatures even higher.

ii. Reactant Pressure

Increased reactant pressure caused particle sizes to increase and caused the compositions of Si_3N_4 powders to be more nearly stoichiometric.

Analysis of the process showed that the heating rate was independent of the pressure of the optically absorbing species because the absorptivity and heat capacity both change proportionally with pressure. Pressure has less effect on nucleation rate than does temperature, so we would not anticipate that pressure would have any appreciable effect on how far the temperature could be driven beyond the level where nucleation rates become appreciable. This critical temperature level and the corresponding nucleation rates are expected to be essentially independent of relatively small pressure changes.

The results of the depletion volume analysis (Section III-A-3) support this conclusion and explain the particle size dependence on pressure. For the range of pressures examined, the distance between growing nuclei was shown to be approximately constant. The observed particle volumes are directly proportional to the mass of reactant gas within the depletion volumes and so are proportional to pressure.

The reason for increasing nitrogen content with increasing pressure has not been determined. It could be simply that the increased partial pressure of nitrogen-bearing species causes the increasing nitrogen content in the particles. It is also possible that the particle growth rates will increase with increasing reactant partial pressures. Consequently, the rate at which

11

exothermic heat is liberated by the growing particles will increase with pressure, causing the particle temperatures to be proportionally higher. As was already shown, higher reaction temperatures cause the particles to be more nearly stoichiometric. Pyrometric temperature measurements did indicate that the flame temperature rose with increasing pressure.

iii. Other Variables

The gas velocity, the NH_3/SiH_4 ratio in the gas, and the dilution with argon had negligible effets on particle characteristics. The absence of an apparent gas velocity effect can be anticipated because the instantaneous heating rates at the reaction temperature change by only a factor of 2-3 in the range of gas velocities investigated. This variation would probably not influence nucleation rates. This same conclusion probably applies to the gas composition and dilution effects.

It is apparent that particle size is insensitive to process variables other than laser intensity and pressure in the ranges of conditions studied. Stoichiometry is manipulatable in an orderly manner; powders can be made which range from mostly pure Si to stoichiometric Si_3N_4 compositions. All as-synthesized Si_3N_4 powders have been amorphous to date, but they crystallize rapidly at temperatures in excess of 1400°C. Silicon powders made from SiH_4 can be either amorphous or crystalline depending on laser intensity. It appears that we should be able to simultaneously achieve virtually all of the ideal powder characteristics which were sought while retaining some control over individual powder characteristics. The continued research has investigated the means of extending the achievable range of particle sizes while retaining the narrow particle size distributions.

b. Summary

This process has easily achieved its primary objective. Powders which result from the laser heated gas phase synthesis process have most of the characteristics presumed to be ideal for ceramic powders. The process also appears capable of reducing the cost of these powders because it requires very little energy per kilogram of powder and utilizes feed materials very efficiently. The process must be investigated further to eliminate the tendency to form chain-like agglomerates and to increase the mean particle size. For many materials, it is desirable to have mean particle sizes of approximately 1000 Å, rather than 250 Å as is typically produced by this

12

process with Si_3N_4. Achieving a larger particle size will require an improved understanding of the nucleation and growth processes. It is also important to apply the process to other materials. Processing of many electronic, magnetic, and optical ceramic materials would benefit from using powders with the characteristics demonstrated in this research program.

2. Particle Size and Shape Modification

Controlled modification of particle size and shape by subjecting powders to high intensity laser illumination was successfully demonstrated in this phase of the first year's work[2]. Selective heating causes particle size reduction by vaporization until decoupling occurs when the oversize particles reach a specific dimension. This approach was based on the diameter dependence of the absorption efficiency (Q_{abs}) of electromagnetic radiation which small particles exhibit.

The Mie theory[5] shows that above a specific diameter, the particles absorb heat with a high efficiency that is independent of diameter. Below a specific diameter, the absorption efficiency decreases with diameter so the particles effectively decouple from the radiation. The absorption efficiency calculated for Si_3N_4 particles is shown in Figure 3. This characteristic permits selective interaction with oversize particles. Their size can be reduced if they are heated long enough to cause considerable vaporization. Oversized particles can be eliminated from the powder, thus avoiding subsequent problems with discontinuous grain growth and strength limiting flaws associated with the oversized grains. Once the particles begin to decouple and cool down, the vaporization rate will effectively stop.

Process models were developed[2] which gave reasonably good agreement between analytical and observed experimental results. They indicated that two vaporization processes probably occur. At the highest intensities, Si_3N_4 particles vaporize as $Si(g)$ and $N_2(g)$. At lower intensities, they apparently decompose by losing $N_2(g)$, leaving molten Si.

The intensity-time exposures required to cause particle size reduction were substantially more severe than predicted in our original analysis. Achieving the process with a 150 watt laser was only marginally possible. Most of the mapping of conditions which caused comminution was done with supported particles in a pulsed laser mode. In this manner, longer and

13
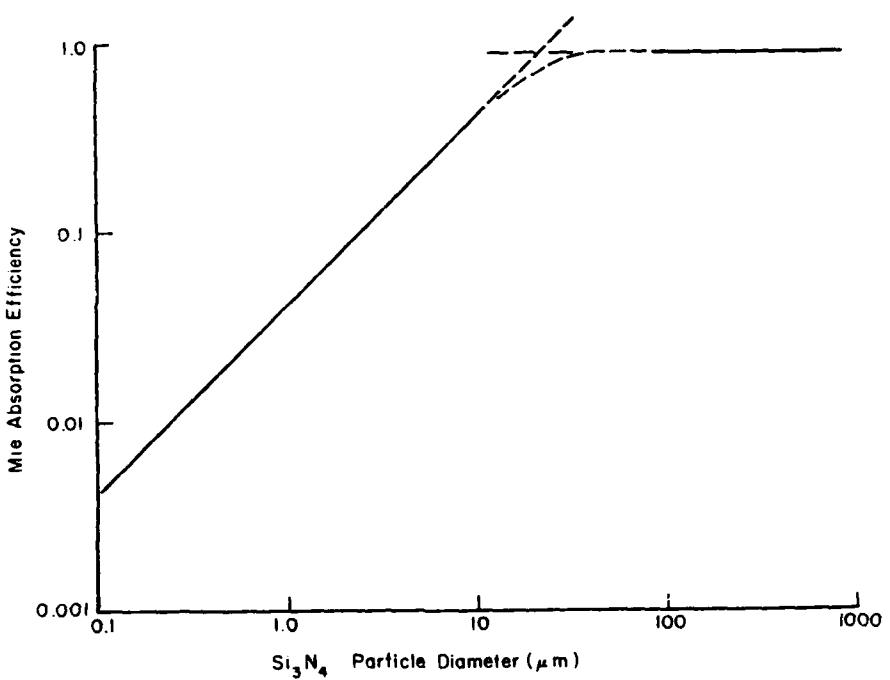
Figure 3. Mie absorption efficiency of Si_3N_4 particles to 10.6 μm
light as function of particle size.

higher intensity exposures were realized than could be achieved with CW, gas
entrained experiments.

These experiments demonstrated particle size reduction, leaving
equiaxed particles. They did not unequivocally demonstrate decoupling,
which will cause the predicted termination of the comminution process at a
specific particle size. Some of the results suggested that all of the
experiments were carried out in the domain where coupling efficiency was
dependent on particle size. These experiments could not be completed
because of the power limits imposed by then existing laser equipment. The
pulsed experiments showed that the process should operate as a CW, gas
entrained process with approximately a 1.5 kW laser, power levels which are
available with equipment we have recently acquired.

14

III   PROCESS RESEARCH CONDUCTED DURING YEAR THREE

The character of this research program has changed considerably from its inception. Initially, the concepts of forming powders by laser induced reactions and of selectively comminuting particles had not been demonstrated. The program was viewed as having a high risk of not functioning as anticipated and most of the experiments were empirical. Since then it has been shown that the synthesis process works extremely well and produces powders with most of the desired characteristics. With this evolution, the program has progressively focused more on analysis and modeling to describe the nature of the process and to determine how to achieve a wide range of particle characteristics. Also, we have begun to process the resulting powders into test specimens. While the comminution process was demonstrated successfully the first year, it was apparent that the laser equipment which was available to the program lacked adequate power. Thus, investigation of this process was deferred.

During the third year, we addressed issues in two general areas. These areas are developing both a better description and better control of the synthesis process, and developing powder processing procedures. The specific topics in the first include:

- characterizing the optical properties of reactant gases
- measuring reaction temperatures
- determining the relationship between process variables and powder characteristics
- modifying equipment
- investigating factors causing agglomeration.

The second area includes:

- developing dispersion methodologies
- investigating shaping processes including cold pressing, isostatic pressing and centrifugal casting
- densifying shaped samples by sintering, and nitriding.

There are many other topics which needed to be addressed, but these were deferred until the fourth year.

A. Synthesis Process

   1. Optical Absorptivities

   The optical absorption coefficients (α) of the reactant gases determine the fraction of the incident laser power absorbed by the gas. This determines heating rates and the overall efficiency of the process. Also, the accuracy with which the particle synthesis process can be modeled depends on how precisely α is known. The effective absorption coefficient is a function of the overlap between the absorption spectrum of the reactant gases and the emission spectrum of the laser. Since the high power CO_2 lasers emit almost totally at the P(20) line at 10.591 μm (944.195 cm^{-1}), it is α at this wavelength that is most important.

   The low pressure absorption spectra of gases such as silane and ammonia are made up of many narrow absorption lines spaced at somewhat regular intervals. Since it is highly unlikely that a single absorption line will have exactly the same wavelength as an emission line of the laser, the difference between the positions of the two lines and their respective line widths will determine α. At low pressures ($<$ 1 torr), Doppler broadening determines the width of the absorption line. The Doppler width, $\Delta\nu_D$, can be calculated from[6]:

$$\Delta\nu_D = 7.16 \times 10^{-7} \left(\frac{T}{M}\right)^{1/2} \nu_o \qquad (cm^{-1})$$

where T is the temperature, M the molecular weight, and ν_o the line center in cm^{-1}. The absorption coefficient at position ν is equal to[6]:

$$\alpha_\nu = \alpha_o \exp - \left[\frac{2(\nu-\nu_o)(\ln 2)^{1/2}}{\Delta\nu_D}\right]^2$$

where α_o is the coefficient at the line center. As the line broadens with increasing temperature, α_o decreases such that the integrated absorption, S, remains constant:

16

$$S = \int \alpha_\nu d\nu = \left(\frac{\pi}{\ln 2}\right)^{1/2} \left(\frac{\Delta\nu_D}{2}\right)\alpha_o = \text{constant}$$

The absorbtivity is very small if the absorption and emission lines are more than a few Doppler widths apart. As an example, the SiH_4 absorption line nearest the P(20) CO_2 line[7] is at 944.213 cm^{-1}, thus the positional difference is only 0.018 cm^{-1}. The calculated Doppler widths of this absorption line are 2.1 x 10^{-3} cm^{-1} at 300K and 4.6 x 10^{-3} cm^{-1} at 1500K, with the resulting values of α_ν being about 10^{-91} α_o and 10^{-18} α_o, respectively. From these values, it is obvious that for silane at low pressures, any absorption will be an artifact due to rare isotopes of silicon in the silane or forbidden energy transitions.

At system pressures above a few torr, collisions between the gas molecules cause the absorption line widths to broaden. For many gases, this broadening, $\Delta\nu_L$, has been found empirically to be proportional to the system pressure[6]:

$$\Delta\nu_L = kP$$

In the presence of pressure broadening, and when $\Delta\nu_L \gg \Delta\nu_D$, the absorptivity can be approximated by[6]:

$$\alpha_\nu = \left[\alpha_o\left(\frac{1}{\pi\ln 2}\right)^{1/2}\frac{\Delta\nu_D}{\Delta\nu_L}\right]\left[\frac{1}{1 + \dfrac{\left(2(\nu - \nu_o)\right)^2}{\Delta\nu_L}}\right]$$

The first term in brackets is the absorption at the peak; it is inversely proportional to pressure. When $(\nu - \nu_o) = \Delta\nu_L/2$, the absorptivity at position has its maximum value:

$$\alpha_{max} = \frac{\alpha_o}{4}\left(\frac{1}{\pi\ln 2}\right)^{1/2}\frac{\nu_D}{(\nu - \nu_o)}$$

In the case of silane, $\alpha_{10.6\mu m\ (max)} = 0.01\ \alpha_o$ at 300K.

The intense laser radiation can change the absorptivity of the gas through simple heating, or by excited vibrational levels. At room temperature virtually all of the gas molecules are in the ground vibrational level, and they are distributed among approximately twenty rotational levels according to a Boltzmann distribution. As the gas is heated, some rotational levels experience an increase in population, and others experience a loss. Since only one rotational level of the ground vibrational level absorbs the laser radiation, changes in the gas temperatures will change the number of molecules that are capable of absorbing the monochromatic light. Although the exact rotational quantum number of the absorbing level in silane is not known, it is apparently higher than the room temperature average. An increase in temperature will therefore increase the silane absorptivity.

Whenever an infrared photon is absorbed, a molecule makes a transition to an excited vibrational level. Collisions soon return this molecule to the ground state, but in the mean time it is unable to absorb another photon unless a transition between the first and second excited vibrational levels is also resonant with the 10.6 µm radiation. Since the spacing between excited vibrational levels in silane is unknown, it is impossible to predict whether a large degree of vibrational excitation will increase or decrease the absorptivity of silane. This will have to be experimentally determined.

Previous absorption measurements[2,3], Figures 4 and 5, were conducted at high laser intensities and over long path lengths (10 cm). They indicated that silane was the strongest absorbing species, that α_{SiH_4} depended strongly on pressure and perhaps on laser power, and that α_{NH_3} was only weakly dependent on pressure and laser intensity. A survey of the SiH_4 absorptivities at other CO_2 laser lines was made using a tunable laser. These indicated that the P(20) line was the most strongly absorbed line and that there were other lines where α_{NH_3} was equal to or greater than α_{SiH_4}. These results indicated that more complete data was required to describe the high pressure, high temperature absorptivities found under conditions used in the particle synthesis with the P(20) emission. An even broader systematic study of the absorptivity as a function of pressure, temperature and/or laser intensity would have to be undertaken to characterize the other absorption lines.
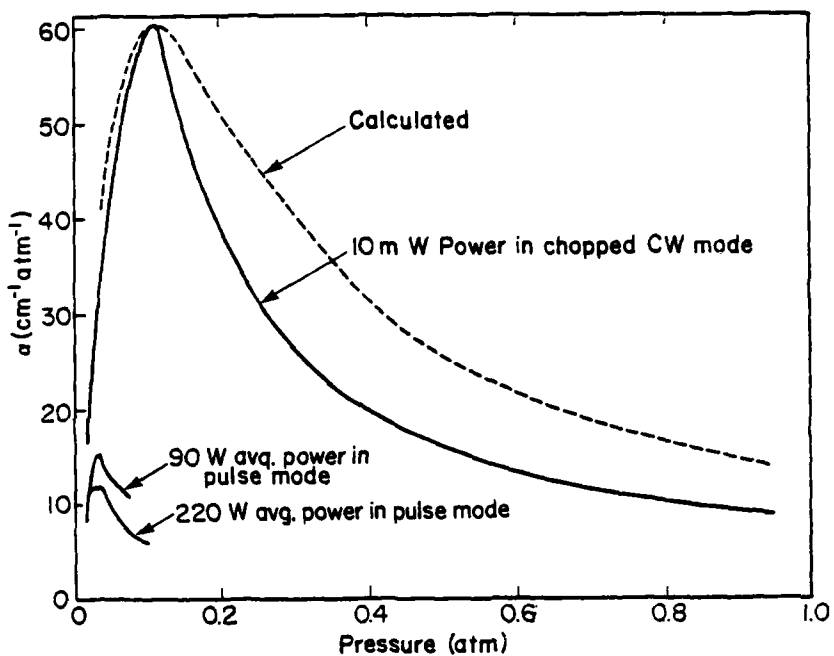
Figure 4. The absorption coefficient of SiH_4 as a function of
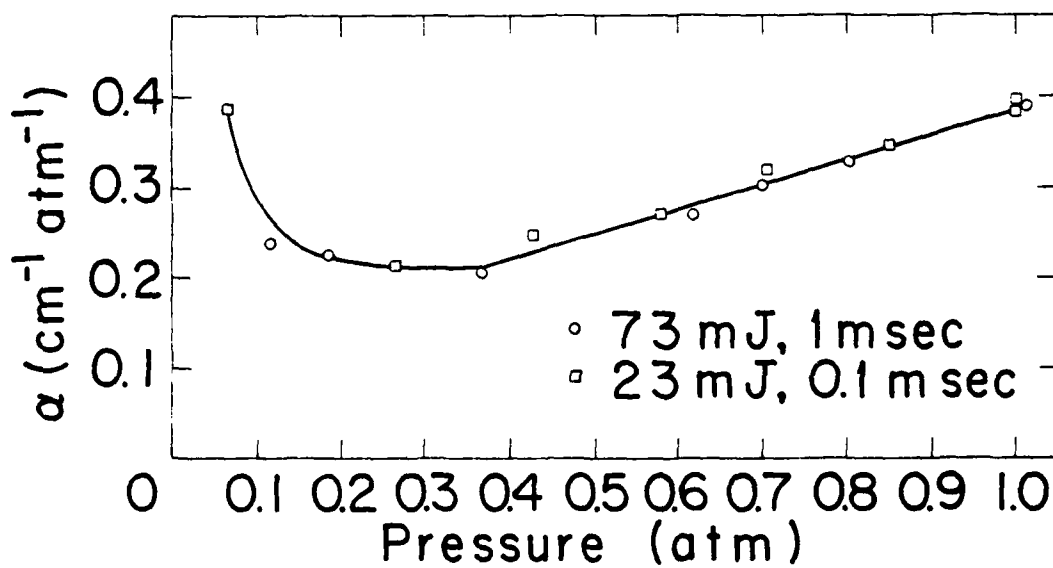pressure for the P(20) CO_2 laser line.

Figure 5. The absorption coefficients of NH_3 as a function of
pressure for the P(18) and P(20) CO_2 laser lines.

New measurements of the silane absorption for the P(20) line under low laser intensity have been made using a 1.2 cm long absorption cell. The 150 watt CO_2 laser was attenuated to 10 milliwatts by three sequential reflections from KCl windows. The transmitted laser energy was detected with a pyroelectric detector coupled to an oscilloscope and a lockin amplifier operated in the AC volts RMS mode. The results are presented in Figure 4 along with previous measurements. The strong dependence on pressure is expected based on the equation for α_ν. A curve of α_ν calculated from this equation using the experimental peak of $\alpha_{SiH_4} = 60$ (atm $\cdot$ cm)$^{-1}$ at 85 torr is also included in Figure 4. Agreement between the experimental and calculated absorptivities is good up to the peak, but the experimental absorptivity falls off more rapidly than expected. This may be due to a small amount of non-P(20) emission from the laser that is not absorbed by the silane. If so, a repeat of the low intensity measurement with a still shorter cell will reveal the true high pressure absorption.

In spite of this uncertainty, the data show that α_{SiH_4} is strongly dependent on laser intensity and/or temperature. Silane couples very strongly to the P(20) line, especially at low intensities. In the fourth year, experiments are planned to determine the exact dependence of α_{SiH_4} on laser intensity from 10 mW/cm^2 to 100 W/cm^2, as well as its low intensity dependence on temperatures up to 400°C. These measurements will determine the extent to which saturation caused the observed strong dependence on intensity, and should allow the development of an accurate model of the laser heating process.

2. Temperature Measurements

Spectroscopic studies intended to determine the particle temperatures within the reaction flame are important both for modeling the reaction process and for providing a means of improving quality control.

The relationship between the intensity of emitted radiation at a given wavelength and the tempeature of the radiating body is described by Wein's approximation of Planck's law[8]:

$$I_\lambda = \frac{C_1 \epsilon_\lambda \, \exp(-C_2/\lambda T)}{\lambda^5} \, d\lambda d\Omega$$

20

where ϵ_λ is the emissivity at wavelength λ, C_1 and C_2 are known radiation constants, and $d\lambda$ and $d\Omega$ are the wavelength and solid angle intervals of the detector. By combining the constants C, $d\lambda$, and $d\Omega$ into a new constant C' and rearranging, one obtains:

$$\ln(I_\lambda \lambda^5) = \frac{-C_2}{\lambda T} + \ln \epsilon_\lambda + \ln C' .$$

If ϵ_λ is independent of λ, then a plot of $\ln(I_\lambda \lambda^5)$ vs. $1/\lambda$ will yield a straight line with a slope of $-C_2/T$, thus permitting the temperature to be calculated. If ϵ_λ is dependent on λ, the functional relationship between these parameters must be determined before the absolute temperature can be calculated.

The emissivity of a flame containing small hot particles can be separated into two parts: the electronic emissivity, $\epsilon_{\lambda e}$, which is dependent on the chemical composition of the particles, and the aerosol emissivity, $\epsilon_{\lambda a}$, which is dependent on the size and the density of the particles in the flame. Kirchhoff's law states that at radiative equilibrium, the emissivity of a body is equal to its absorptivity. The absorptivity, and thus the emissivity, of silicon increases very strongly from the red to the blue end of the spectrum[9]. The intensity of the flame will therefore be higher in blue than in red compared with that expected for an opaque black body at the same temperature. Thus, the color temperature of the flame, which depends on the distribution of intensity with wavelength rather than the absolute intensity at each wavelength, will be higher than its true temperature. A similar effect also results because the radiating particles are smaller than the wavelength of the light they are emitting. The absorption efficiency of a small particle can be derived from Mie scattering theory.[5] For small particles of a uniformly absorbing (black) material, the emissivity is proportional to $1/\lambda$; that is, $\epsilon_{\lambda a}$ is greater at the blue end than at the red end of the spectrum.

It should be expected, therefore, that the relative emissivity of the SiH_4 flame will fall somewhere between following a $1/\lambda$ dependence and following the room temperature silicon particle absorption spectrum. Calculating the temperature from the spectral emittance of the flame with the first dependence results in the maximum calculated temperature and the

21

second results in the minimum calculated temperature. Whatever the dependence of ε_{λ_e} with λ, it should remain constant as long as silicon is the dominant emitter. Since stoichiometric silicon nitride is transparent in the visible region of the spectrum, the silane-ammonia flame emittance will be due to the excess silicon in the particles. The temperature measurements for both silane flames and silane-ammonia flames are therefore evaluated using silicon emissivity corrections. The magnitude of the aerosol emissivity, ε_{λ_a}, will depend on the size of the particles and on their density in the flame as well as the wavelength. It will therefore depend on those reaction conditions that affect particle size and density such as mass flow rate and total pressure. It will not be constant, and could vary strongly from run to run.

Measurements of the silicon particle absorption coefficient were made at room tempeature using a well dispersed suspension of silicon powder in n-propanol. In these measurements, the particles were well separated and expected to interact with light through Rayleigh scattering. It was assumed that light scattering is small compared to absorption and that absoprtion was not strongly affected by the n-propanol medium (although the absorption of n-propanol per se was subtracted out, Rayleigh scattering also considers the relative index of refraction and extinction coefficient between the particles and the media). The results of this measurement were used to calculate the electronic emissivity.

Temperature measurements of the reaction flame involve two related but distinct techniques. The first measures the emittance of the radiation from the flame at a single wavelength. The second measures the relative emittances of the flame at several wavelengths. The first technique requires a calibrated detector, and the detector constants, $d\lambda$ and $d\Omega$. An optical pyrometer avoids these specific problems by superimposing the image of the body on a heated filament. The temperature of the body is determined when it and the filament have equal intensities as observed by eye. ε_λ must be determined to permit calculation of the true temperature. Without this emissivity correction, the temperature measured with the pyrometer underestimates the true flame temperature by as much as several hundred degrees. This is because this technique assumes ε_λ is equal to 1 at the wavelength used, when, in fact, it is always substantially less than 1 due to the combined effects of electronic and aerosol emissivities.

The second technique involves measuring the relative emittance of the flame at several wavelengths. Only the relative emissivities and a detector calibrated with respect to wavelength are needed since the ratios of the emittances at different wavelengths are measured.

Previously reported spectra[2,3] of typical silane and silane-ammonia flames recorded with a monochromator-photomultiplier (PMT) combination are presented in Figure 6. The data have been corrected for detector sensitivity as a function of wavelength. ε_λ was assumed to be constant in this plot. It took about 30 minutes to read each complete spectrum because these spectra contain many points. Since the flame intensity often varies substantially in this time period, this method is too slow for routine temperature monitoring.

An optical multichannel analyzer (OMA) is a much more rapid means of collecting the flame spectrum. An OMA II, on loan from Princeton Applied Research, was used to study the flame under a variety of conditions. Representative data are presented in Figure 7. The OMA II disperses the flame spectrum onto a vidicon, where the entire spectrum is recorded simultaneously. The data can be collected in a couple of minutes, and any flame fluctuations affect all wavelengths equally. However, the red edge of the spectrum is limited by the vidicon sensitivity to around 0.650 μm, and the complete system is too expensive to be used as a dedicated temperature monitor.

The combined limitations of the PMT-monochromator system and of the OMA-II led to the development of a PMT-interference filter detector system that allows routine monitoring of the reaction flame temperature. The photomultiplier is an RCA C31034 QUANTACON which is sensitive to 0.850 μm. A rotating wheel holding interference filters which transmit at 0.449 μm, 0.548 μm, 0.658 μm and 0.801 μm is mounted on the front of the PMT tube housing. This permits rapid monitoring of the flame at these four wavelengths by observation of the PMT signal on a digital voltmeter or a chart recorder. Early data from three silane-ammonia flames are presented in Figure 8. Again, near linear plots result.

Flame temperatures deduced from the above measurements are presented in Table II. The data have been evaluated two ways: one assuming black particle emissivity ($\varepsilon_\lambda \propto 1/\lambda$), and the other assuming emissivity proportional to our measured absorptivity of a sample of silicon powder
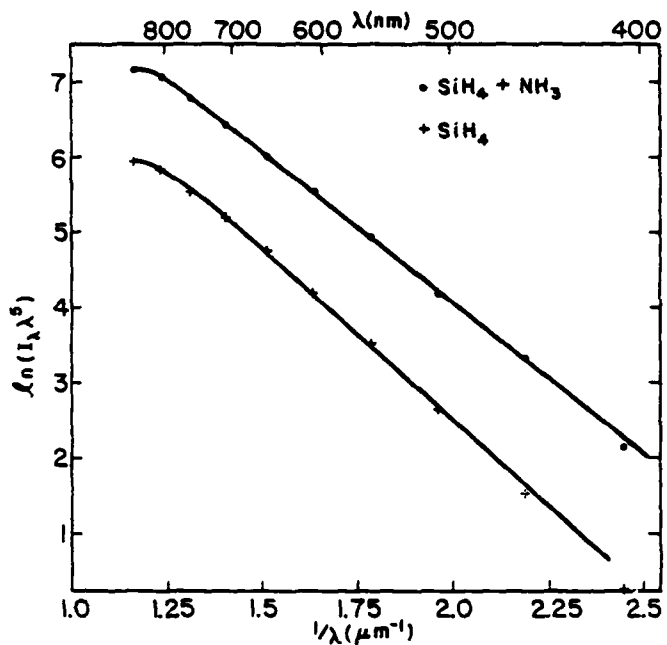
23

Figure 6.   Emission spectra (plotted as $\ln(I_\lambda \lambda^5)$ vs. $1/\lambda$) of reaction flame measured with a monochromator-photomultiplier detector.
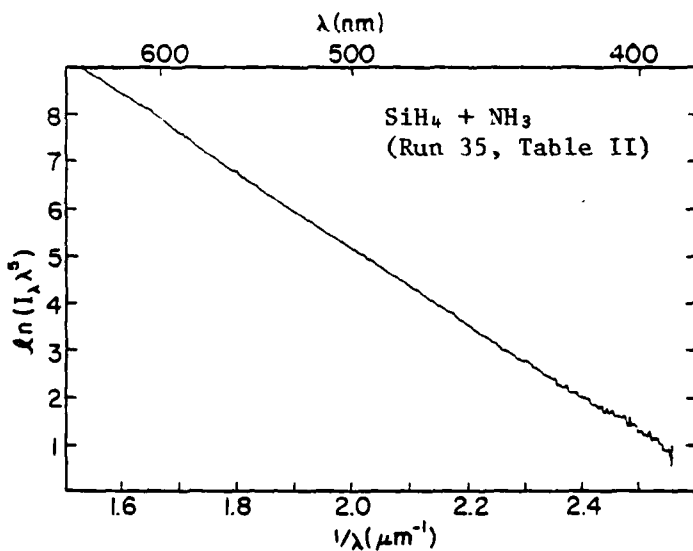

Figure 7.   Emission spectra (plotted as $\ln(I_\lambda \lambda^5)$ vs. $1/\lambda$) of reaction flame measured with an optical multichannel analyzer (OMA).

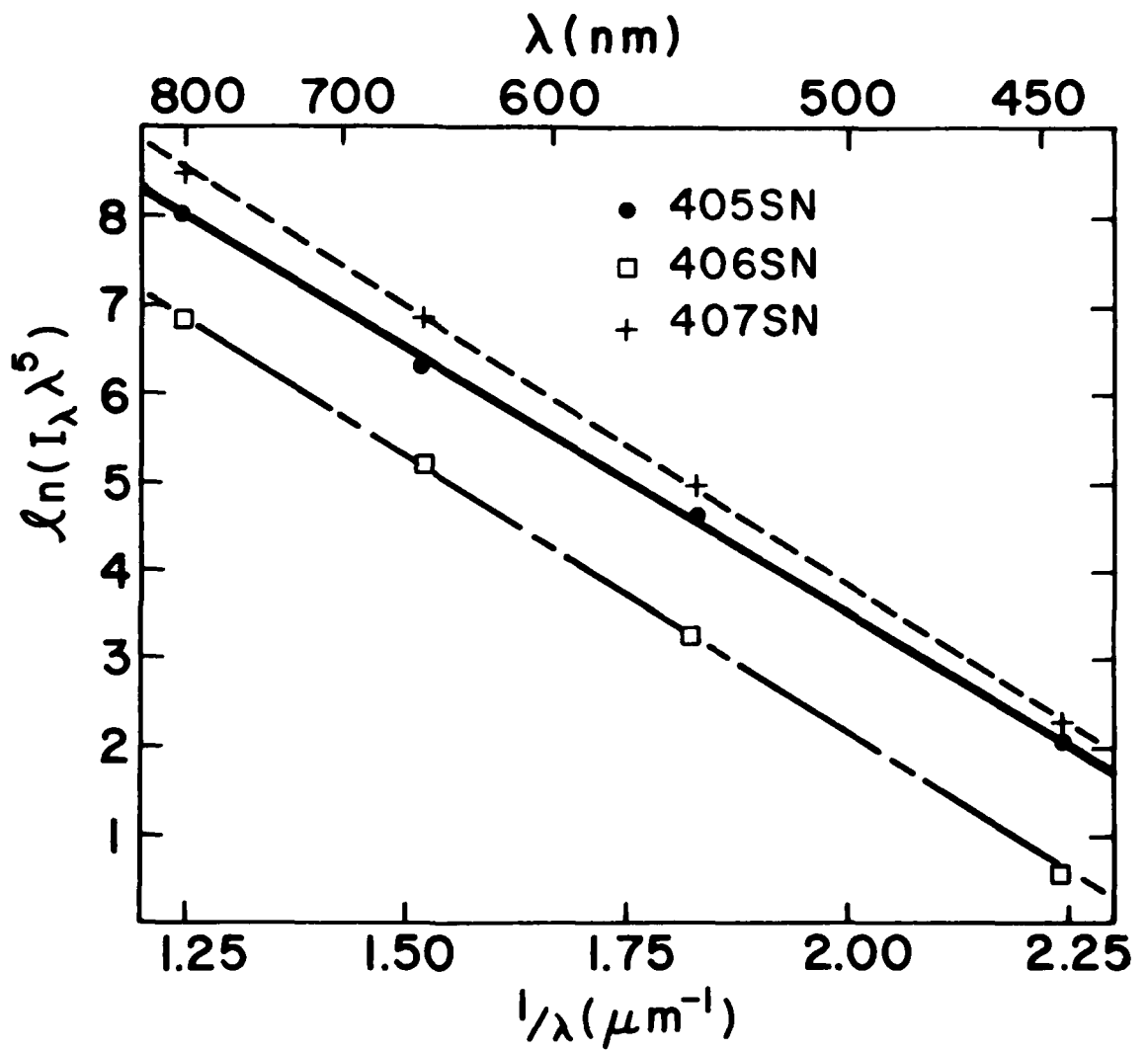Figure 8. Emission spectra (plotted as $\ln(I_\lambda \lambda^5)$ vs. $1/\lambda$) of reaction flame measured with a photomultiplier-interference filter detector.

(α_{Si}). Unfortunately, only the last three runs presented have been studied with both the pyrometer and the PMT-filter detector. The run conditions are included to allow further comparison between the two techniques.

Pyrometer readings, uncorrected for emissivity, generally range from 800 to 1100°C for silane flames, and from 950 to 1300°C for silane-ammonia flames (see Sections III-A-3-a and III-A-3-b). If $\varepsilon_{0.65\mu m} = 0.1$ is used to correct these temperature ranges, they become 935 to 1329°C for silane flames, and 1128 to 1608°C for silane-ammonia flames.

As Table II indicates, the temperatures derived from the relative emittance experiments cover a wide range depending on what emissivity dependence is assumed. Setting ε_{λ} equal to the measured room temperature absorptivity of Si particles results in calculated temperatures that are close to the uncorrected pyrometer temperatures. This agreement is not meaningful since the pyrometer temperatures were calculated assuing $\varepsilon_{.65\mu m} = 1$, whereas the relative emission temperatures were calculated assuming $\varepsilon_{.65\mu m} \leqslant 0.1$. If the pyrometer temperatures are recalculated assuming $\varepsilon_{.65\mu m} = 0.1$, the new pyrometer temperatures no longer agree with the relative temperature measurements. The conclusion must be that the pyrometer readings are low, and that the room temperature absorption of silicon varies more strongly than its high temperature absportion. At high temperatures, valence electrons are thermally promoted to the conduction band, where they cause the Si to partially exhibit the uniform emissivity characteristics of metals. The temperature at which silicon begins to exhibit this uniform emissivity is unknown, and thus further research is planned to improve the values of ε_{λ} used to calculate the absolute temperature.

Relative emittance measurements provide a means of measuring relative temperature levels which are free from the effects of varying particle densities within the flame. The following conclusions can therefore be drawn: (1) the flame temperature is a sensitive function of gas flow rates and total pressure, but in a way that is not yet obvious; (2) the higher laser intensities increase the flame temperature; and (3) the optical pyrometer readings are sensitive to flame density and do not provide a simple measure of relative temperatures. Accurate and reliable relative temperatures can be measured easily with the PMT-interference filter method, and absolute temperatures should be available soon.

TABLE II

Summary of Reaction Temperature Estimates by Various Techniques

Run	Laser Intensity (watts/cm^2)	Pressure (torr)	Flow Rates (cc/min)		Temperature (°C)			
					Pyrometer		OMA or PMT	
			SiH$_4$	NH$_3$	$\epsilon=1$	$\epsilon=.1$	$\epsilon_\lambda=1/\lambda$	$\epsilon_\lambda=Si_{abs}$
PMT-Monochrometer*								
Silane Flame	887	115	19	–	–	–	1125	839
SiH$_4$-NH$_3$ Flame	887	245	11	110	–	–	1413	1001
OMA-II**								
31	810	147	11	78	–	–	1302	936
33	810	357	11	117	–	–	1252	907
35	810	607	8	100	–	–	1377	980
37	810	615	11	111	–	–	1384	984
39	887	610	11	104	–	–	1430	1010
43	887	152	11	106	–	–	1112	820
45	887	152	11	100	–	–	1086	804
47	887	152	4.5	22	–	–	1034	773
49	887	590	19	223	–	–	1250	916
88	2×10^4	150	4.5	51	–	–	847	651
90	2×10^4	85	4.5	43	–	–	847	651
94	2×10^4	400	4.5	60	–	–	1326	950
99	880	430	9	68	–	–	1438	1014
98	887	430	9	68	–	–	1881	1250
54	887	432	9	68	–	–	1476	1035
56	887	432	9	68	–	–	1569	1087
PMT – Filters								
405SN	2×10^4	570	40	87	1230	1509	1895	1239
406SN	2×10^4	570	19	93	1107	1338	1840	1212
407SN	2×10^4	490	40	86	1165	1418	1820	1203

* Powder Not Collected

** SiH$_4$-NH$_3$ Flame, Powder Not Collected

3. Effect of Process Variables on Powder Characteristics

One of the ultimate objectives of this program is to develop an understanding of the relationships, based on equilibrium thermodynamics and kinetics, between the laser heated gas phase reaction and the resulting powder characteristics. During the first two years of the program, the effects that process variables such as laser intensity, cell pressure, gas velocity and gas mixture, have on the reaction and resulting powder characteristics were studied almost exclusively for Si_3N_4 powder synthesis. We have continued this study of the Si_3N_4 synthesis and have begun a more detailed investigation of the Si powder synthesis from direct pyrolysis of SiH_4 and SiH_4-Ar mixtures. The process characteristics are summarized in Appendix I and the resulting powder characteristics are summarized in Appendix II. It is anticipated that the results of these studies along with an improved understanding of the reaction temperature and reactant gas absorptivities and velocities will permit a quantitative description of the synthesis process based on classical homogeneous nucleation and growth theory.

   a. Silicon Powders

      i. Powder Synthesis Experiments

      ● Gas velocity

Two sets of experimental runs were performed with pure SiH_4 (Ar was used as the annular and window gas) to examine the effect of reactant gas velocity. These runs are summarized in Table III. The powders were synthesized at either 0.20 atm or 0.35 atm. The velocity was altered by changing the volumetric flow rate of SiH_4.

The effect of velocity on the reaction zone temperature (as determined by the optical pyrometric technique) is shown graphically in Figures 9 and 10 at pressures of 0.20 atm and 0.35 atm, respectively. Also shown in these figures is the equivalent spherical diameter calculated from BET surface area measurements. In Figure 9, both curves exhibit an ascending-descending behavior with the largest sized particles resulting from reaction zone having the highest temperature. Figure 10 shows that the particle size of powders produced at 0.35 atm follows the same trend. There is insufficient data at 0.35 atm to demonstrate conclusively that the reaction zone temperature dependence on gas velocity is the same as that at 0.20 atm.

28

Figure 9.   The effect of velocity on the silicon synthesis reaction
flame temperature and resulting powder particle size
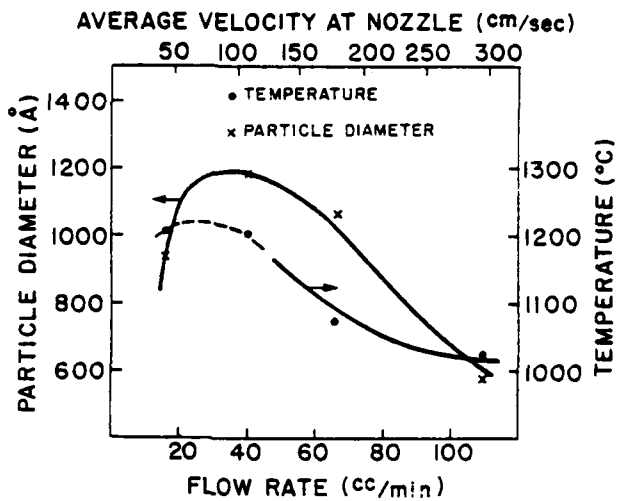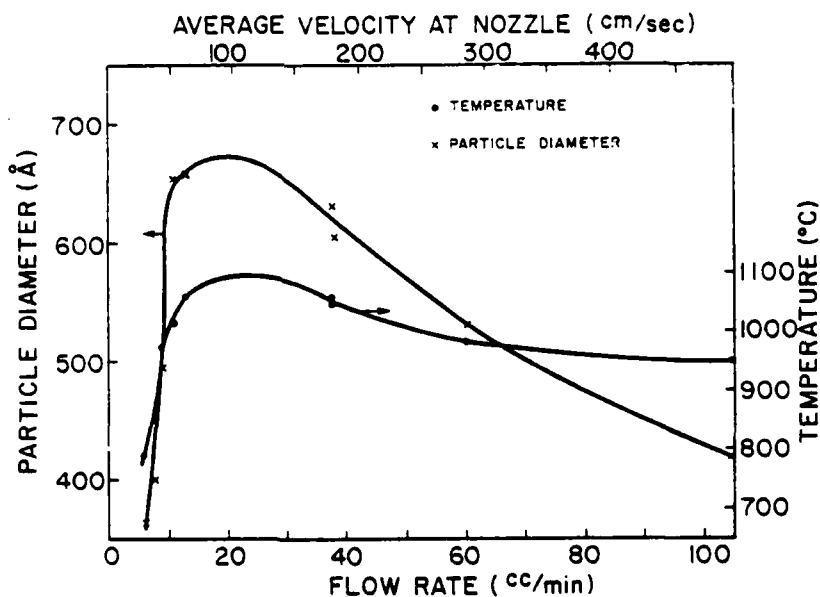(reaction cell pressure of 0.20 atm).

Figure 10.   The effect of velocity on the silicon synthesis reaction
flame temperature and resulting powder particle size
(reaction cell pressure of 0.35 atm).

TABLE III

Effect of Reactant Gas Velocity on the Si Synthesis Process

Run	Flow Rate (cc/min)	Temp. (°C)	BET		Crystallite Size (Å)	$\dfrac{d_{BET}}{d_{X\text{-ray}}}$	Conversion Efficiency (%)
			Area (m^2/g)	Equiv. Size (Å)			
629S*	5.5	790	70	367	84	4.4	85
627S*	7.5	850	64	402	118	3.4	90
628S*	8.8	950	53	486	145	3.4	100
625S*	11	1030	39	660	172	3.8	92
626S*	13	1065	39	660	214	3.1	92
631S*	38	1055	43	599	175	3.4	87
632S*	38	1045	41	628	178	3.5	88
633S*	60	980	49	526	149	3.5	90
630S*	104	950	61	422	131	3.2	98
636S**	16	1215	28	920	263	3.5	86
624S**	40	1200	22	1160	344	3.4	100
622S**	66	1055	25	1046	306	3.4	90
623S**	110	1025	46	567	175	3.2	100

*For each run: Pressure = 0.20 atm, Intensity = 764 W/cm^2
**For each run: Pressure = 0.35 atm, Intensity = 865 W/cm^2

The efficiency with which the SiH_4 gas is converted to powder in the reaction zone ranged from 80-100%. It did not appear to be a function of reactant gas stream velocity.

The Si powders were crystalline to both X-ray and electron diffraction. The crystallite size was determined from X-ray diffraction peak broadening using a 1.0 μm Al_2O_3 powder as an internal standard. Table III shows the calculated crystallite diameter along with the ratio of the BET particle size to the crystallite size, $\dfrac{d\ BET}{d\ x\text{-ray}}$. For all but one run, the particle

diameter is approximately 3.5 times larger than the crystallite size. For run 629S, having the lowest reactant gas flow rate $\left(5.5 \frac{cc\ SiH_4}{min}\right)$, the ratio is significantly larger $\left(\frac{d\ BET}{d\ x\text{-ray}} = 4.4\right)$ than for the other powders. At this time, it is not evident whether this difference can be attributed directly to the slow reactant flow rate; it may result from the lower reaction temperature.

Figure 11 shows a TEM micrograph of powder produced in run 631S. The average particle size measured from this micrograph is 525 Å ± 59 Å, which is in fair agreement with the BET size (609 Å). In general, the BET equivalent spherical diameter and the diameter measured from TEM micrographs have always been nearly equal, indicating that the particles have smooth surfaces and no porosity accessible to the surface.

Figure 12 shows the Si powder 630S produced with the highest SiH_4 flow rate (104 cc/min) investigated. Once again, the average particle size measured from the micrograph (366 Å) is in good agreement with the BET equivalent diameter (418 Å). The particle size distribution for this powder, ranging from 255 to 436 Å, is narrower than for silicon powders made with slower reactant gas velocities. This might be a consequence of the reaction occuring further into the laser beam and the particle traveling through the beam at a faster rate, so that the nucleation and growth of the particles to their final size occurs in a shorter time interval (see heating rate curve, Figure 15).

Two runs (631S and 632S) were performed using identical process conditions to examine the reproducibility of the laser synthesis process. The reaction zone and resulting powder characteristics are summarized in Table IV. The reaction temperatures and conversion efficiencies are nearly identical. The equivalent size from BET surface area measurements and the crystallite size measured by X-ray line broadening were also in excellent agreement. These results show that the process is easily controllable and can produce powders with similar characteristics from run to run. It should be noted that many of the earlier Si powders were made with SiH_4 flow rates of about 10 cc/min. It is evident from Figures 9 and 10 that in this regime, the reaction zone and particle characteristics exhibit large variations with small changes in flow rate. The differences previously reported between powders synthesized with these lower, nominally identical,

31

1000 Å

1000 Å

Figure 11. TEM photomicrograph of Si powders from lot 631S.

Figure 12. TEM photomicrograph of Si powders from lot 630S.
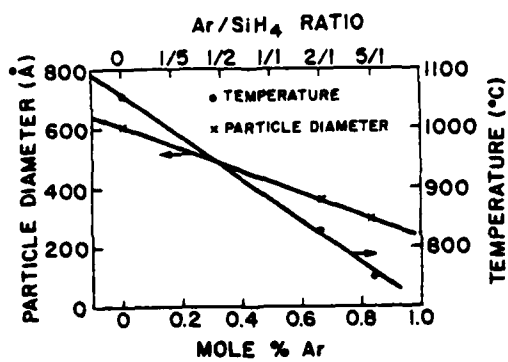
Figure 13. The effect of the Ar/SiH₄ ratio in the reactant gas stream on the silicon synthesis reaction flame temperature and resulting powder particle size.

1000 Å

Figure 14. TEM photomicrograph of Si powders in lot 634S.

TABLE IV

Comparison of Two Identical Synthesis Runs

Run	Flow Rate (cc/min)	Laser Intensity (W/cm²)	Pressure (atm)	BET Area (m²/g)	BET Equiv. Size (Å)	Temp. (°C)	Crystallite Size (Å)	$\frac{d_{BET}}{d_{X-ray}}$	Conversion Efficiency (%)
631S	38	764	0.20	43	599	1055	175	3.4	87
632S	38	764	0.20	41	628	1045	178	3.5	88

33

SiH$_4$ flow rates are probably attributable to inaccuracies in the measurement of the reactant gas flow rates.

Spectrographic analyses have indicated that the powders are predominantly pure Si with the total cation impurities typically less than 200 ppm. The oxygen content is generally less than 1.0% by weight and some runs have produced powder with an O$_2$ concentration as low as 0.05 wt. %. The purity of the resulting powders varies somewhat from run to run, but it does not seem to be dependent on the specific run conditions. Rather, it is related to experimental procedures such as outgassing time, vacuum tightness of the cell and post-production handling of the powder.

● Ar dilution

Four runs (631S, 632S, 634S and 637S) were made to examine the effect of diluting the reactant gas stream with argon. Runs 631S and 632S were made under the identical conditions with the reactant gas stream comprised of pure SiH$_4$ to serve as a benchmark from which the effect of dilution could be compared. Run 634S had an Ar/SiH$_4$ molar ratio of 5/1 (83 mole % Ar) and run 635S had a ratio of 2/1 (67 mole % Ar). The process conditions for these runs as well as the resulting reaction zone and powder characteristics are summarized in Table V.

The effect of dilution on the reaction zone temperature and the equivalent spherical particle size determined by BET surface area measurements are shown in Figure 13. Both the reaction zone temperature and particle size decreased with increasing dilution of the gas stream with argon. The conversion efficiency ranged from 80-87% and it is not evident that the conversion is systematically dependent on the gas dilution.

The crystallite sizes of powders synthesized from runs 631S and 632S were discussed in the previous section. For these, the ratio of the BET equivalent size to the crystallite diameter was approximately 3.5. The diffraction patterns for powders 634S (5/1 Ar/SiH$_4$) and 637S (2/1 Ar/SiH$_4$) showed only very broad peaks centered at angles corresponding to the d-spacings of the (111) and (220) reflections of silicon. This suggests the particles are either comprised of very fine crystallites or are amorphous. An amorphous structure may be a consequence of the low reaction temperatures.

Figure 14 shows a TEM micrograph of powder 634S (5/1 Ar/SiH$_4$ ratio). The average particle size measured from this micrograph is 275 Å, which is

TABLE V

Effect of Argon Dilution on the Si Synthesis Process*

Run	Ar/SiH$_4$ Ratio	Mole % Ar	BET Area (m²/g)	BET Equiv. Size (Å)	Temp. (°C)	Crystallite Size (Å)	$\frac{d_{BET}}{d}$ X-ray	Conversion Efficiency (%)
631S	0	0	43	599	1055	175	3.4	87
632S	0	0	41	628	1045	178	3.5	88
637S	2/1	67	72	358	830	Amorphous	–	86
634S	5/1	83	88	293	750	Amorphous	–	80

* For each run: Pressure = 0.20 atm, Intensity = 764 W/cm^2, Total reactant flow rate = 38 cc/min.

TABLE VI

Effect of Laser Intensity on the Si Synthesis Process*

Run	Laser Intensity (W/cm²)	BET Area (m²/g)	BET Equiv. Size (Å)	Temp. (°C)	Crystallite Size (Å)	$\frac{d_{BET}}{d}$ X-ray	Conversion Efficiency (%)
622S	865	25	1046	1055	306	3.4	90
635S	764	31	823	–	–	–	89
638S	380	68	379	930	Amorphous	–	98

*For each run: Pressure = 0.35 atm, SiH$_4$ flow rate = 66 cc/min.

in close agreement with the BET equivalent diameter of 294 Å. The particle size appears to be quite uniform, ranging from 189 Å to 355 Å. It was anticipated that diluting the gas stream with Ar would decrease the probability of collision between particles and thus reduce the particle agglomeration. Figure 14 shows that the powder produced with this dilution still exhibits the typical two-dimensional chain-like agglomerates, with significant necking between particles. Agglomerates are discussed more fully in Section III-A-3-c.

- Laser Intensity

Three runs (622S, 635S, 638S) in which all proce variables were held constant except laser intensity are summarized in Table VI. The average intensity ranged from 380 W/cm^2 (638S) to 865 W/cm^2 (622S). The reaction zone temperature (by optical pyrometry) increased as the intensity increased. A pyrometer temperature reading was not taken for run 635S because the reaction cell windows became covered with powder before the reaction stabilized. The particle size increased significantly as the intensity was increased. This behavior is directly opposite to the results of the synthesis of Si_3N_4 from NH_3-SiH_4 gas mixtures where the particle size decreased with increasing laser intensity.

The conversion efficiency ranged from 89% to 98%. The results do not suggest any systematic dependence on laser intensity. X-ray diffraction patterns revealed that powders produced with intensities of 865 W/cm^2 and 764 W/cm^2 (622S and 635S) had similar crystal structures. The ratios of particle size calculated from BET surface area measurements to the crystallite size calculated from X-ray line broadening are almost identical $\left(\frac{d\ BET}{d\ X\text{-ray}} = 3.46 \text{ and } \frac{d\ BET}{d\ X\text{-ray}} = 3.30 \text{ for runs 622S and 635S, respectively} \right)$. X-ray diffraction analysis of the powder produced at 380 W/cm^2 (638S) did not show a crystalline pattern, which suggests they are amorphous. This is consistent with our earlier work[2,3] where lower intensities produced amorphous Si powders.

- Pressure

As indicated previously, two series of runs were done to determine the effect of gas velocity on the laser synthesis process. The two series were made at 0.20 and 0.35 atm pressure so that the effect of pressure on the reaction zone and resulting powder characteristics could be investigated. Comparison of Figures 9 and 10 shows that increased pressure leads to both

an increased particle size and a higher reaction temperature. Since the two series of runs used slightly different laser intensities, it can not be concluded that the effects are attributable solely to the changes in pressure.

The effect of pressure on the silane molecule density in the gas stream and the relationship between pressure and the final particle size is discussed in terms of the reaction depletion volume in the following section. At this time, it is not known whether the apparently higher reaction temperature is an explicit result of the change in process parameters or whether it is related to the higher density of SiH_4 within the gas stream, e.g. a denser stream of particles may increase the brightness observed by pyrometry (see Section III-A-2 on the reaction zone temperature). The change in pressure did not appear to effect the crystallite size calculated from X-ray diffraction line broadening.

ii. Analysis and Discussion

• Heating Rates

The time-temperature history of the reactant gases as they travel through the laser beam has been calculated by procedures described in the 1979 Annual Report[3]. Figure 15 shows the effect of velocity on heating rates for gas volume elements traveling along the central axis of the gas stream through the maximum laser intensity. The four curves correspond to run 629S (silane flow rate = 5.5 cm^3/min), 625S (11 cm^3/min), 631S (38 cm^3/min) and 630S (104 cm^3/min), at a cell pressure at 0.2 atm. The gas volume elements are assumed to contain pure SiH_4, that is, there is no dilution of the gas stream by the argon gas flowing over the KCl window or through the annular sleeve. An average value was used for the SiH_4 absorption coefficient (7.5 $(atm-cm)^{-1}$) and it was assumed to be independent of temperature. We have evidence that this may not be an entirely accurate assumption (see Section III-A-1), but at present there is insufficient data to determine the actual dependence of the absorptivity on temperature.

For all of these velocities, the heating rate analysis predicts that the gases should reach temperatures in excess of 1000°C before reaching the maximum laser intensity at the center of the laser beam. For run 625S (having a SiH_4 flow rate of 5.5 cm^2/min), the reactant gas is heated to 1200°C after it has traveled only 0.025 cm into the 0.5 cm diameter laser beam. For run 630S (110 cm^3/min SiH_4), the reactant gas is heated to 1200°C

after traveling 0.20 cm into the 0.5 cm diameter beam. For this run, the reaction flame had a shape similar to that reported previously[3], with the upper cusp of the flame located at approximately 0.2 cm into the laser beam. For the lower flow rates, the flame did not exhibit the characteristic cusp. It appeared that the lower flame boundary was coincident with the beginning of the laser beam. In all cases, the reaction was initiated before the reactant gases penetrated to the centerline of the laser beam where the intensity reaches its maximum.

Figure 15 shows that both average heating rates and instantaneous heating rates at the temperature level where silane pyrolyzes rapidly, approximately 1000K, increase with increasing reactant gas flow rate. It is anticipated that higher instantaneous heating rates will force the reaction temperature to higher levels, so the faster SiH_4 flow rates should produce a higher reaction temperature. This is not in agreement with the ascending-descending temperature dependence (measured by optical pyrometer) on reactant gas flow shown in Figure 9. It should be noted that this heating rate analysis does not consider the exothermic heat released during the pyrolysis reaction. This effect will be considered briefly in a later section.

Figure 16 shows the calculated heating rates for gas elements traveling along the gas stream axis for run conditions corresponding to runs 631S, 634S and 637S. These illustrate that diluting the reactant gas stream with Ar affects two critical parameters which determine the gas heating rate. First, it decreases the absorption coefficient of the gas stream since Ar is essentially nonabsorbing at a wavelength of approximately 10.6 μm. Second, the heat capacity is changed significantly since the heat capacity of SiH_4 is 3 to 4 times greater than that of Ar. These two effects act in opposite directions. Combined, they produce a less pronounced effect than if the reactant gas stream was diluted with a non-absorbing species having a heat capacity simila. to that of SiH_4. Figure 16 shows that both the average heating rate and the instantaneous heating rate decrease as the reactant gas stream is diluted with argon. The instantaneous heating rates do not change very much because the diluted reactants penetrate closer to the centerline of the laser beam when they reach the reaction temperature, therefore, the local laser intensity is higher.
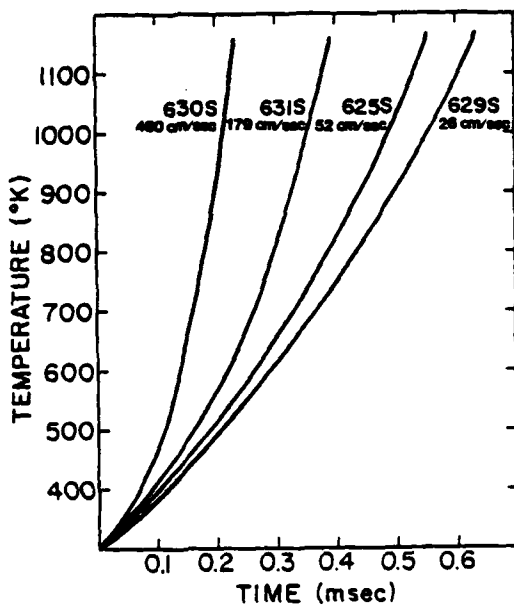
Figure 15. The effect of velocity on the calculated temperature of the reactant gases during Si synthesis.
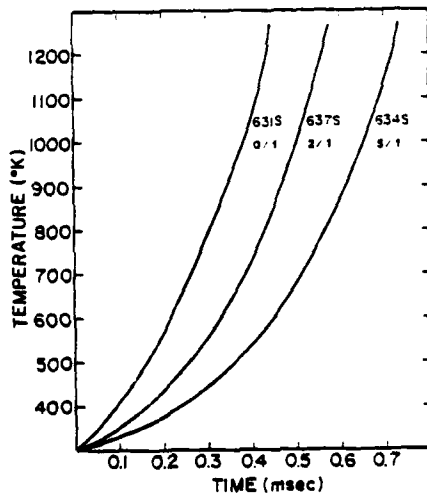

Figure 16. The effect of Ar/SiH₄ ratio on the calculated temperature of the reactant gases during Si synthesis.

39

The analysis showed the gas heating rate will be independent of pressure[3] for gas streams that are optically thin. In a highly absorbing gas stream, the laser beam will be progressively absorbed as it passes through the gas stream, causing differences in thermal histories between gas elements on the entering and exiting sides of the gas stream. This heating rate analysis also assumed that the optical absorptivities are not dependent on pressure. This is not precisely valid as shown in Section III-A-1. The data required to provide a more accurate model is not yet available, so it is not possible to predict pressure effects on heating rates with any more accuracy.

- Depletion volume

Once the reactant gases reach the reaction temperature, nuclei begin to form and grow within the gas stream. As far as we can determine[3], this point coincides with the beginning of the visible flame. We have shown that the conversion efficiency of the reaction mass is nearly 100% for the silicon synthesis runs discussed in this section. Since the silane is almost completely depleted from the reactant gas stream, particle growth is not limited by elapsed growth time but by the depletion of the silane between neighboring particles. The depletion volume is calculated by comparing the mass of silicon in a particle with the mass density of silicon atoms in the gas stream. The calculated depletion volumes were adjusted to take into account the actual conversion efficiencies.

The calculated depletion volumes for silicon synthesis runs are summarized in Figures 17, 18, 19, and 20. In general, the depletion volumes range from about 1.4×10^{-11} cm^3 to 6.84×10^{-13} cm^3, corresponding to entrained particle densities in the gas stream of 7.14×10^{10} to 1.46×10^{12} particles/cm^3 depending upon the actual run conditions. The particle density is a direct measure of the number of nucleation events which occur before impingement.

Figures 17 and 18 show the effect of flow velocity on the depletion volume for the runs corresponding to pressure of 0.20 and 0.35 atm, respectively. The similarity of these curves to Figures 9 and 10 suggests that lower temperatures produce smaller depletion volumes and thus a smaller particle size.

Figure 19 shows the effect of argon dilution on the depletion volume. Once again lower reaction temperatures produced smaller depletion volumes.
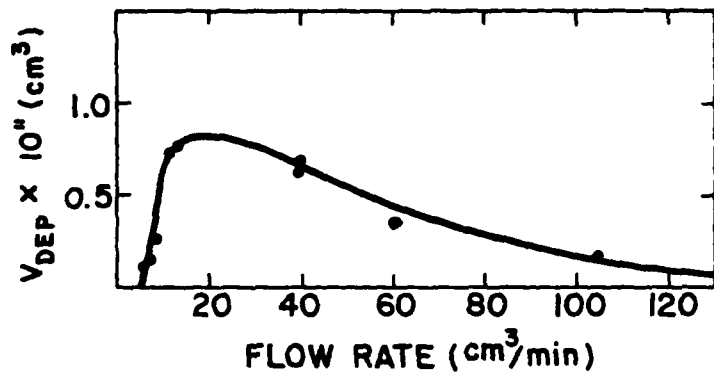
Figure 17. The effect of reactant flow velocity on the gas depletion volume for Si synthesis (reaction cell pressure of 0.2 atm).
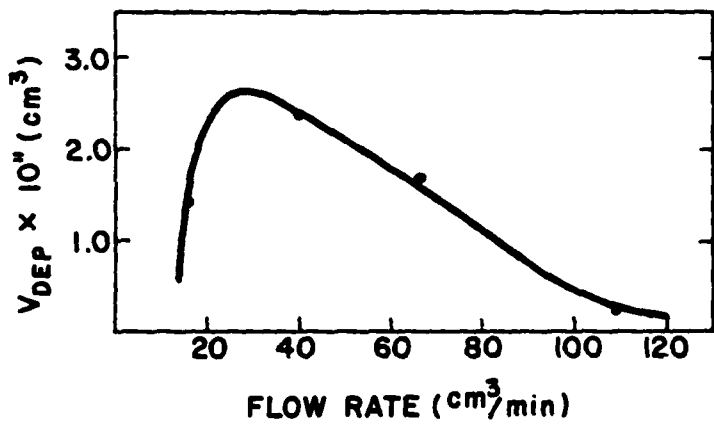

Figure 18. The effect of reactant flow velocity on the gas depletion volume for Si synthesis (reaction cell pressure of 0.35 atm).

41

As the Ar/SiH_4 ratio increases the depletion volume decreases. Also, the density of silane molecules in the gas stream decreases by a factor of 3 for run 637S (2/1 AR/SiH_4) and by a factor of 6 for run 634S (5/1 Ar/SiH_4). The combination of these effects indicates why the particle size decreased with argon dilution as shown in Figure 13.

Figure 20 shows the effect of laser intensity on the depletion volume. Laser intensity produced the greatest effect on this characteristic of the process. Powder made with an intensity of 380 W/cm^2 (638S) had a depletion volume of 6.84×10^{-13} cm^3 while that produced with 865 W/cm^2 (622S) had a volume of 1.73×10^{-11} cm^3.

The effect that pressure has on the depletion volume is indicated by comparing Figures 17 and 18. The depletion volume increased by a factor of 2 to 3 as the reaction cell pressure was increased from 0. J atm to 0.35 atm. Since the runs made at 0.35 atm used intensity of 8u5 W/cm^2 while those done at 0.2 atm were produced with intensity of 760 W/cm^2, it is not certain that the increase in depletion volume is a consequence of the change in pressure. As shown in Figure 20, rather small variations in laser intensity produced relatively large variations in depletion volume. If the depletion volume was not significantly changed by small variations in pressure with all other process parameters held constant, we would expect the particle volume to be directly proportional to the pressure, since the density of silane molecules in the reactant gas stream is directly proportional to the pressure.

The relationship between temperature and depletion volume observed for SiH_4 is directly opposite to that observed for Si_3N_4 synthesis from SiH_4-NH_3 gas mixtures. This indicates the relative temperature dependences of the nucleation and growth rates are different for these two synthesis processes.

- Exothermic Heat Released.

The previous heating rate analyses did not include the effect of latent heat associated with the pyrolysis of SiH_4 to form Si powder. In fact, they are thermal analyses of the process up to the point that the reaction just begins. The following simple calculations permit conclusions to be made regarding both the possibility of a self-sustaining reaction without continued input of energy from the laser as well as the anticipated maximum temperature rise in the reaction products.
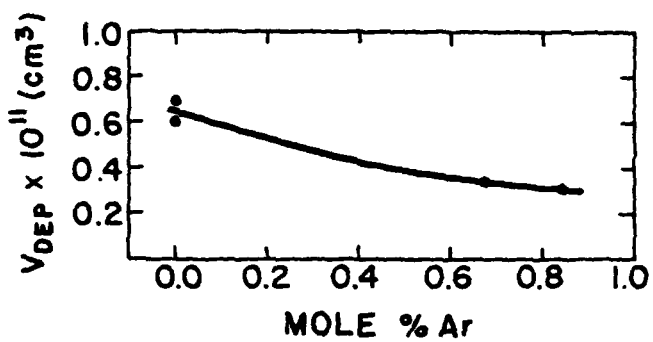
Figure 19. The effect of Ar/SiH_4 ratio on the gas depletion volume for Si synthesis.
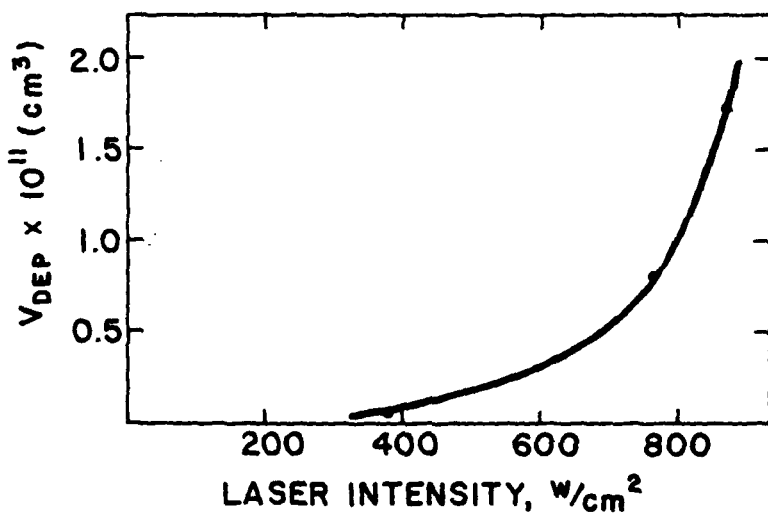

Figure 20. The effect of laser intensity on the gas depletion volume for Si synthesis.

To a first approximation, a reaction can be self-sustaining only if the latent heat released during the reaction exceeds the sensible heat required to raise the reactants to a temperature level where the reaction proceeds rapidly. For the silane pyrolysis reaction

$$SiH_4(g) \rightarrow Si(s) + 2H_2(g)$$
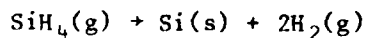
at 1100K, the latent heat is $\Delta H = 2.14 \times 10^4$ J/mole and the sensible heat required to raise the gas to this temperature is 5.76×10^4 J/mole. With 90% conversion efficiency, the effective latent heat (1.93×10^4 J/mole) is less than the sensible heat. This reaction cannot be self sustaining unless the reaction is induced at a much lower temperature. With the same conversion efficiency, we estimate that the adiabatic temperature rise in the excess reactants and reaction products would be approximately 180°C.[3]

    b. Silicon Nitride Powders

        i. Powder Synthesis Experiments

        ● Gas Velocity

Three experimental runs (4113SN, 4114SN and 4115SN) were performed to examine the effect of reactant gas velocity on the Si_3N_4 synthesis process and the resulting powder characteristics. In these runs, the cell pressure (0.75 atm), laser intensity (764 W/cm^2) and NH_3/SiH_4 ratio (2/1) were held constant. The total reactant gas flow rate was changed from 21.5 to 198 cm^3/min. The process conditions and resulting reaction zone and powder characteristics are summarized in Table VII.

As the reactant gas stream velocity was increased, the reaction zone temperature (by optical pyrometry) also increased. The particle size, as determined from BET surface area measurements, decreased slightly with increasing velocity.

        ● NH_3/SiH_4 Ratio

Three runs (4113SN, 4112SN, and 4111SN) were performed to further investigate the effect of the NH_3/SiH_4 gas ratio on the reaction zone and particle characteristics. Previous studies[3] (runs 614SN, 603SN and 615SN) examined only a small range of NH_3/SiH_4 ratios (5/1, 10/1 and 20/1, respectively). In the more recent runs (4113SN, 4112SN, and 4111SN), the NH_3/SiH_4 ratio was changed from 2/1 to 43/1 while all other process

TABLE VII

Effect of Reactant Gas Velocity on the Si_3N_4 Synthesis Process*

Run	Total Reactant Gas Flow Rate (cm^3/min)	Av. Reactant Gas Velocity at Nozzle (cm/sec)	Temp. (°C)	Surf. Area (m^2/g)	Particle Diameter (Å)	Depletion Volume (cm^3)
4113SN	198	248	1400	79.8	268	2.3×10^{-13}
4114SN	66	83	1310	73.9	289	2.9×10^{-13}
4115SN	21.5	27	1260	68.4	312	3.7×10^{-13}

* For each run: Pressure = 0.75 atm, NH_3/SiH_4 ratio = 2/1,
Intensity = 764 W/cm^2.

parameters were held constant, e.g. cell pressure (0.75 atm), laser intensity (764 W/cm^2) and total reactant gas flow rate (198 cm^3/min). These runs are summarized in Table VIII.

One of the major effects of changing the NH_3/SiH_4 ratio is to alter the absorptivity within the reactant gas stream since the absorption coefficient for SiH_4 at the wavelength of the laser emission is much larger than that for NH_3 (see Section III-A-1). This effect will be discussed in terms of reactant gas heating rates in the following section. The reaction zone temperature, as determined by optical pyrometry, decreased as the NH_3/SiH_4 ratio was increased. This is in agreement with previous results[3] (runs 614SN, 603SN and 615SN). The particle size, as determined from BET surface area measurements, also decreased as the NH_3/SiH_4 ratio was increased. The relationship between the final particle size and both the density of silane molecules in the reactant gas stream and gas depletion volume will be discussed in the next section since the stated correlation between Si_3N_4 particle size and reaction temperature is not followed in this case. The previously reported runs[3] (614SN, 603SN, and 615SN) did not appear to exhibit a particle size dependence on the NH_3/SiH_4 ratio. This may have been because the range of NH_3/SiH_4 ratios examined was fairly small (from 5/1 to 20/1).

TABLE VIII

Effect of NH_3/SiH_4 Ratio on the Si_3N_4 Synthesis Process*

Run	NH_3/SiH_4 Ratio	Temperature (°C)	Surface Area (m^2/g)	Particle Diameter (A)	Depletion Volume (cm^3)
4111SN	43	850	138.	156	7.3×10^{-13}
4112SN	10	1030	87.5	244	6.4×10^{-13}
4113SN	2	1400	79.8	270	2.3×10^{-13}

* For each run: Pressure = 0.75 atm, Intensity = 764 W/cm^2,

Reactant Gas Flow Rate = 198 cm^3/min.

ii. Analysis and Discussion

● Heating Rate

Figure 21 shows the effect of the NH_3/SiH_4 ratio on the calculated heating rates for reactant gas volume elements traveling along the central axis of the gas stream through the maximum laser intensity. The three curves correspond to run conditions 4111SN, 4112SN and 4113SN (Table VIII). Both the instantaneous gas heating rate at the point where the reaction was initiated (estimated by measuring the position in the laser beam where the reaction flame begins) and the average gas heating rate up to this point increased as the NH_3/SiH_4 ratio is decreased. The position in the beam where the reaction was first observed was not measured for run 4111SN, but the heating rate analysis suggests that the reaction temperature for this run cannot be higher than 900K.

All of the calculated reaction temperatures for the Si_3N_4 synthesis process predicted by this heating rate analysis are lower than both the measured temperature (by optical pyrometry) and the reaction temperature of SiH_4/NH_3 gas mixtures reported in the literature[15]. Our analysis does not include the effect of exothermic heat released during the reaction. Also, the quantitative validity of this analysis is limited primarily by the uncertainty in the values used for the reactant absorptivities. Nonetheless this analysis provides useful qualitative insight into the effect the process parameters have on the reactant gas heating rates.

46

Figure 22 shows the calculated effect of gas velocity on heating rates for reactant gas volume elements traveling along the central axis of the gas stream. Increasing velocity causes increases in both the average heating rate and instantaneous heating rate at the point where the reaction is initiated. In fact, for the slowest velocity (run 4115SN), the reaction was initiated so soon after the reactant gas entered the laser beam, that the beginning of the flame and the laser beam were nearly coincident. Thus, in this case, the gas was heated to the reaction temperature well before it experienced the maximum laser intensity.

In both sets of data, the calculated reation temperature was qualitatively consistent with the temperature measured by optical pyrometry. That is, the reaction temperature increased as the reactant gas velocity was increased or as the NH_3/SiH_4 ratio was decreased. By including the temperature increase due to the exothermic reaction and developing a better understanding of the reactant gas stream velocities and absorptivities, we hope to be able to resolve the quantitative differences in the measured and calculated reaction temperatures.

● Depletion Volume

The calculated depletion volumes for the two sets of Si_3N_4 synthesis runs are also shown in Tables VII and VIII. These volumes were calculated by relating the mass of silicon in a single particle to the mass density of silicon atoms in the reactant gas stream. The particle density within the gas stream is inversely proportional to the depletion volume. If we assume that each nucleus grows independently, then the particle density is equal to the nucleus density. Therefore, the depletion volume calculations can be used to provide insight in the nucleation of the particles within the reactant gas stream.

Examination of Table VII shows that the depletion volume decreased slightly as the reactant gas stream velocity was increased. This result suggests that the nucleation rate increased slightly with increased velocity and the correspondingly increased reaction temperature.

Table VIII shows that the depletion volume increased as the NH_3/SiH_4 ratio was increased. Since we changed the NH_3/SiH_4 ratio at constant pressure, the density of silane molecules in the reactant gas stream was altered for each of these runs. This explains the observed particle size dependence. Even though the gas depletion volume increased with an increase
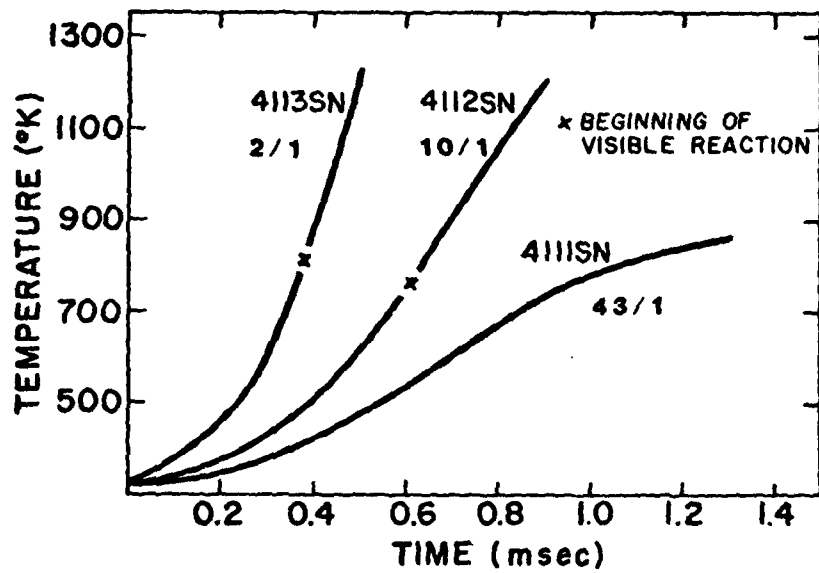
47

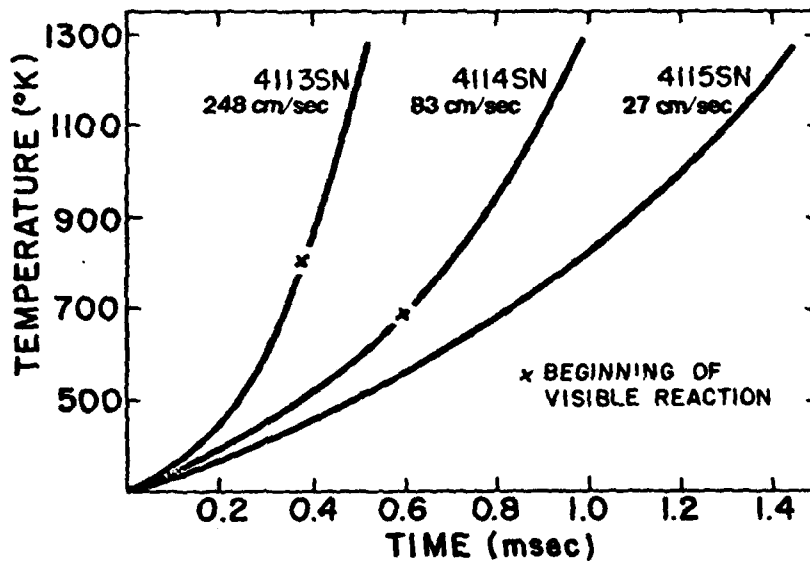Figure 21. The effect of NH_3/SiH_4 ratio on the calculated temperature of the reactant gases during Si_3N_4 synthesis.

Figure 22. The effect of velocity on the calculated temperature of the reactant gases during Si_3N_4 synthesis.

in the NH_3/SiH_4 ratio, the molar density of silane in the gas stream decreased by a proportionally larger amount and thus the final particle size decreased.

Examination of Tables VII and VIII shows that an increased reaction temperature produces a decrease in the depletion volume. This suggests that the nucleation rate increases at a proportionally larger amount than the growth rate as the reaction temperature is increased. This is the same as was observed previously[3] with Si_3N_4 and as shown, is opposite to that observed for the synthesis of silicon from pure SiH_4 and SiH_4/inert gas mixtures (see Section III-A-3-a).

c. Particle Agglomeration

TEM analysis has shown that all of the laser synthesized powders (Si, Si_3N_4 and SiC) exhibit agglomeration characterized by two-dimensional networks of particles. The majority of the Si powders also appear to have neck formation between the particles. This necking has not been observed in the Si_3N_4 or SiC powders.

When fine particles collide, van der Waals forces will act to join the particles and form agglomerates. Once contact is made between the particles, additional forces may make their separation difficult. Contacting particles can reduce their exposed surface by deforming, creating a contact area between them. The decrease in surface energy acts as a bond. The radius of the contact area can be estimated by assuming elastic deformation. If material is actually transferred from the particles to the neck region between the joined particles by either diffusional or evaporation-condensation mechanisms, a sintered aggregate may be formed. Two theoretical situations have been examined to investigate the agglomeration issue: frequency of particle collisions and the neck formation between the particles by elastic deformation due to a decrease in the surface free energy.

i. Particle collisions

Brownian motion and fluid shear are two principle mechanisms by which particle collisions can occur. Each of these collision rates can be influenced by inter-particle forces such as van der Waals forces and Coulombic forces.

49

● Collision induced by Brownian motion

For particles that are much smaller than the mean free path of the gas molecules, the collision frequency due to Brownian motion is[10]:

$$F(t) = \left(\frac{192 \ kTr}{\rho}\right)^{1/2} N$$

where: ρ is the particle density (g/cm^3)

k is Boltzmann's constant

r is the particle radius (cm)

T is absolute temperature (°K)

N is the particle density within the gas steam ($\#/cm^3$)

and $F(t)$ is the collision frequency of a single particle ($\#/sec$)

The mean free path in argon at 1100K and 0.2 atm (approximately 1.67 x 10^{-4} cm) is one to two orders of magnitude larger than the typical particle size. Thus the use of the above expression for the collision frequency is justified.

For silicon synthesis using the run conditions identical to 631S, $r = 3.025 \times 10^{-6}$ cm, $\rho = 2.33$ g/cm^3, $N = 1.66 \times 10^{11}$ particle/cm^3, $k = 1.38 \times 10^{-16}$ erg/°K, and T = 1323K, the collision frequency is 1120 collisions/ particle · sec. Under these run conditions, the average flow velocity is estimated to be 100 cm/sec and the dwell time of the particles in the flame is 2.4×10^{-2} sec. Thus on the average, a particle will undergo approximately 27 collisions while in the flame and approximately 33 additional collisions before reaching the filter. Van der Waals forces are estimated to increase the collision frequency[11] by a factor of 1.152.

● Fluid shear

In the orthokinetic case, particles flowing in a fluid stream collide because of their relative motion. The collision frequency is given by the following expression[12]:

$$F(t) = \frac{32}{3} r^3 N \frac{du}{dx}$$

where $\frac{du}{dx}$ is the velocity gradient across the gas stream. The parameters r, and $F(t)$ are the same as above. For the Si synthesis conditions used in run 631S, $\frac{du}{dx}$ is estimated from computer results to be 1×10^3 cm/sec·cm. Using the same N and r values given above yields a collision frequency, $F(t)$, of approximately 4.9×10^{-2} collisions/particles ·sec. This indicates that collisions by Brownian motion will dominate.

● Effect of process variables on collision frequency

The particle density in the gas stream is the parameter which dominates the collision frequency caused by Brownian motion. Reaction temperature and particle radius will have less of an effect since the collision frequency has a square root dependence on them. Increased gas stream velocity should reduce the total number of collisions a particle undergoes since the residence time is reduced proportionally.

It was anticipated that diluting the reactant gas stream with argon would decrease the collision frequency by the combined effects of reducing the reaction temperature and the particle density. Runs 631S, 634S and 637S investigated this effect with silane and silane-argon mixtures. Table IX gives the calculated collision frequency for these three runs. The total number of collisions a particle experiences is porportional to the collision frequency since the flow velocity is the same for all three runs.

Table IX shows that the collision fequency did not change significantly with dilution of the gas stream. Even though the reaction temperature decreased as the gas stream was diluted, an effect which by itself would reduce the collision frequency, the density of particles in the gas stream increased because the particles were smaller. Consequently, the collision frequency was not greatly affected by dilution of the gas stream.

ii. Neck formation between particles.

Many of the TEM micrographs show the formation of necks between silicon particles. The fraction of the neck radius which results from cold sintering under the influence of surface forces can be estimated. In this calculation, it is assumed that the necks form by elastic deformation due to surface tension forces. A force balance is used to calculate the resulting

TABLE IX

Calculated Collision Frequency caused by Brownian Motion

Run	Ar (mole %)	T (°K)	r (cm)	$N\left(\dfrac{\text{particles}}{\text{cm}^3}\right)$	$F(t)\left(\dfrac{\text{collisons}}{\text{particle-sec}}\right)$
631S	0	1323	3.025×10^{-6}	1.66×10^{11}	1120
634S	0.833	1032	1.47×10^{-6}	2.86×10^{11}	1183
637S	0.667	1103	1.80×10^{-6}	2.93×10^{11}	1392

radius size. The ratio of the radius of contact area, x, to the particle radius, r, is given by[13]:

$$\frac{x}{r} = \left(\frac{\gamma_{eff}}{0.16\ Er}\right)^{1/3}$$

with

$$\gamma_{eff} = 2\ \gamma_{sv} - \gamma_{ss}$$

where: γ_{eff} = effective interfacial energy

γ_{sv} = interfacial energy between the solid and the vapor phase

γ_{ss} = the grain boundary energy

E   = Young's modulus.

The interfacial energy and grain boundary energy are related by the following expression[14]:

$$\gamma_{ss} = 2\ \gamma_{sv}\ \cos\ (\psi/2)$$

where ψ is the angle of the grain boundary groove. Combining these equations gives:

$$\frac{x}{r} = \left(\frac{2\ \gamma_{sv}(1-\cos\ \psi/2)}{0.16\ Er}\right)^{1/3}$$

52

Using the following values[14]:

$$\psi = 150°$$
$$\gamma_{sv} = 900 \text{ ergs/cm}^2$$
$$E = 1.63 \times 10^{12} \text{ dynes/cm}^2$$
$$r = 2 \times 10^{-6} \text{ cm}$$

$x/r = 0.108$ for a 400 Å particle. This gives a neck diameter of 43 Å for a 400 Å particle, indicating significant neck formation can arise simply from surface forces. Qualitatively, this size is in agreement with observations. Presumably, these necks can be broken by a proper dispersing agent when no bonding has occurred between the particles. Additional neck formation can arise through sintering mechanisms such as evaporation-condensation, surface diffusion, lattice diffusion and grain boundary diffusion. These bonds can not be broken by dispersing agents.

4. Equipment Modifications

During the past year, several modifications of the reaction cell were made. These were done to raise the production rate, improve the yield of usable powder and increase the total capacity per run. Since increasingly more emphasis has been directed toward the processing of the laser synthesized powders into pieces, larger batch sizes are needed.

The capacity for powder collection was increased by replacing the 7.6 cm long filter with one 17.8 cm long. Since making the change, up to 10 g of powder has been collected in the filter from a single synthesis run. Before this modification, the limit was about 5 g of powder before the filter clogged and we were no longer able to maintain a constant pressure.

Previously, only about 50% of the powder were captured in the microporous filter and the other 50% deposited on the walls of the reaction cell. With the longer filter assembly, it is no longer possible to fit both the reaction cell and filter into the antechamber of the glove box. Therefore, two modifications were made to reduce the fraction of powder which remained in the reaction cell and would otherwise be contaminated by exposure to air.

In the original cell design, the argon annular flow was introduced through an inlet tube with a much smaller diameter than the annular sleeve (see Figure 2). An aluminum insert, approximately 4 cm long, comprised of hexagonal cross-sectional tubes with 4 mm openings, was positioned inside the annular sleeve. This modification improved the uniformity of the argon

flow above the annular sleeve. A 6 cm long, 2.5 cm I.D. glass tube was also inserted into the outlet tube, forming a confined path from a position directly above the laser beam all the way to the filter. The purpose of the glass tube was to keep the powder particles entrained in the annular gas stream to the filter assembly. Synthesis runs done with these modifications have essentially 100% of the powder collected in the filter.

A chemical analysis of one Si powder (run 027S) revealed a significant amount of lead (400 ppm) and tin (800 ppm). It was thought that the solder which attached the water-cooled cooper "beam stop" to the reaction cell was the source of this contamination. To avoid this problem in future runs, the copper block was replaced by a KCl window and the beam was arrested outside the reaction cell. This modification provided an additional advantage, since the power of the exiting beam could now be measured while powder was being synthesized. This provided a means of estimating the amount of power absorbed in the reaction zone.

An in-line Ti gettering furnace was installed to reduce the O_2 content in the argon buffer gas. Also, an oxygen analyzer* was connected directly to the synthesis cell, thereby enabling the oxygen partial pressure in the cell to be measured.

B. Powder Processing

1. Powder Dispersion

To produce uniform, dense compacts by processes in which the powder is suspended in a liquid medium, it is essential to create a stable powder dispersion and to rid the powder of agglomerates. It is generally possible to form high quality parts by slip casting, settling or by centrifugal casting from this dipsersed condition. For the special case of using uniform sized spherical powders, it should be possible to create the ordered structures shown in Figure 1. Dispersion experiments were initiated with Si powders to serve as a basis for these fabrication processes. This study is directed toward forming parts of reaction bonded silicon nitride (RBSN).

Early studies on the dispersability of silicon were reported near the beginning of the century. Weiser[16] first reported forming a hydrosol of thoroughly pulverized silicon by treating the powder alternately with acid and alkali. Wegelin[17] also prepared hydrosols of silicon, but by mechanical

---

* Thermox I Analyzer, Ametek, Inc.

grinding. Astfalk and Gutbier[18] investigated chemical preparation of colloidal silicon by reduction of silicon dioxide with magnesium. After grinding and washing the product with hydrochloric acid, they obtained a weak, unstable sol in some cases and, in others, a more concentrated fairly stable sol.

Our initial studies showed that aqueous media have two disadvantages with the laser synthesized Si powders: (1) oxidation of these fine powders is difficult to prevent during drying and (2) when cast from aqueous suspensions, silicon tends to gel, making subsequent elimination of water difficult. We have, therefore, chosen to study dispersions of silicon in various organic solvents. Besides not forming gels, these liquids have the added advantage of being sufficiently volatile that they may be easily eliminated during drying. We have avoided the use of deflocculants because they are difficult to eliminate.

Special care must be taken to control the processing atmosphere because the presence of oxygen influences the wetting properties of powder in the dispersion process. According to Williams and Goodman[19], a single crystal silicon wafer is oxidized immediately when exposed to air and the resulting SiO_2 layer greatly affects the wetting characteristics. In previous investigations on silicon dispersion, the experiments were performed in uncontrolled atmospheres, so there is some ambiguity in the meaning of the results.

    a. Experimental

       i. Materials

The silicon powder used in this study was synthesized from the laser driven decomposition of $SiH_4(g)$ under the reference conditions given in Table I. Single point BET measurement showed the surface area to be 55 m^2/g, corresponding to an equivalent spherical diameter of 465 Å. Neutron activation analysis indicated 0.14 wt % oxygen and spectroscopic analysis indicated < 30 ppm of all other elements. Commercially available grades of the organic liquids were used in this study. The purity specifications for these are given in Table X. Selected physical properties are given in Table XI. Liquids were chosen from as many families as possible. They include aliphatic hydrocarbons, cyclo-aliphatic hydrocarbons, members of the benzene group, alcohols, ketones, ether, aliphatic acids, aldehyde and water. The

TABLE X

Grades and Impurities of the Liquids Used

No.	Liquid	Supplier	Grade	Main Impurities
	Aliphatic Hydrocarbons			
1	n-Hexane	Fisher	Certified	Sulfur Compound, 0.002%
2	Cyclohexane	Mallinckrodt	Analytical	
3	n-Octane	J.T. Baker	Baker	
	Benzene Group			
4	Benzene	Mallinckrodt	Analytical	
5	Toluene	J.T. Baker	Reagent	Sulfur Compound, 0.002%
6	Xylene	Fisher	Cert. (UV)	Sulfur Compound, 0.0006%
	Alcohols			
7	Methanol	Mallinckrodt	Absolute	$(CH_3)_2CO$, 0.001%; CH_3COOH, 0.0018%; Water, 0.02%
8	Ethanol	U.S. Indust.	Absolute	
9	n-Propanol	Mallinckrodt	Analytical	CH_3COOH, 0.015%
10	Isopropanol	Fisher	Certified	Water, 0.1%
11	n-Butanol	Mallinckrodt	Reagent	CH_3COOH 0.001%; Butyl-Ether, <0.02%; Water, 0.05%
12	n-Heptanol	Eastman		
13	n-Octanol	Fisher	Certified	$C_7H_{15}COOH$, 0.01%
14	Benzyl Alcohol	Mallinckrodt	Analytical	C_6H_5CHO, 0.2%
15	Ethylene Glycol	Fisher	Certified	CH_3COOH, 0.004%; Water, 0.2%
	Ketones			
16	Acetone	Mallinckrodt	Analytical	CH_3OH, 0.01%; $(CH_3)_2CHOH$, 0.005%; Water, 0.3%
17	2-Pentanone	J.T. Baker	Baker	
18	2-Heptanone	Aldrich		
	Ether			
19	Isopentyl Ether	J.T. Baker	Baker	
	Aliphatic Acids			
20	Propionic Acid	Fisher	Certified	Water, 0.1%
21	Butyric Acid	Eastman		
	Aldehydes			
22	Benzaldehyde	Baker	Reagent	

TABLE XI

Physical Properties of Liquids[*]

No.	Liquid	Dielectric Constant[7]	Vapor-Liquid Surface Tension[8] (mN/m)	Boiling Point[7] (°C)	Viscosity[7] (cPoise)
	Aliphatic Hydrocarbons				
1	n-Hexane	1.89 a	18.4 a	69.0	0.326 a
2	Cyclohexane	2.02 a	25.2 a	80.7	1.02 b
3	n-Octane	1.95 a	21.6 a	125.7	0.542 a
	Benzene Group				
4	Benzene	2.28 a	28.9 a	80.1	0.652 a
5	Toluene	2.4 c	28.5 a	110.6	0.590 a
6	Xylene	2.3-2.5 a	28-30 a	138-145	0.62-0.81 a
	Alcohols				
7	Methanol	32.6 c	22.5 a	65.0	0.597 a
8	Ethanol	24.3 c	22.4 a	78.5	1.200 a
9	n-Propanol	20.1 c	23.7 a	97.4	2.256 a
10	Isoproponal	18.3 c	21.3 a	82.4	2.86 d
11	n-Butanol	17.8 a	25.4 a	117.3	2.948 a
12	n-Heptanol	-	-	176	8.53 d
13	n-Octanol	10.3 a	27.5 a	194.5	10.6 d
14	Benzyl Alcohol	13.1 a	35.5 a	205.4	5.8 a
15	Ethylene Glycol	38.7 a	48.4 a	197.5	20.5 a
	Ketones				
16	Acetone	20.7 c	25.1 a	56.2	0.316 c
17	2-Pentanone	15.4 a	23.6 a	102	-
18	2-Heptanone	9.8 a	26.7 a	151.5	-
	Ether				
19	Isopentyl Ether	2.82 a	22.9 a	173.2	-
	Aliphatic Acids				
20	Propionic Acid	3.30 e	26.7 a	141.0	1.10 a
21	Butyric Acid	2.97 a	26.5 a	163.5	1.54 a
	Aldehydes				
22	Benzaldehyde	17.8 a	38.5 a	178.1	1.395 c
	Inorganic				
23	Water	78.5 c	72.75 a	100.0	1.002 a

[*] Temperature (°C) at which measurement was made: a = 20°, b = 17°, c = 25°, d = 15°, e = 10°.

single crystal silicon wafer, used for contact angle measurements was boron doped to a level of $10^{17}/cm^3$.

ii. Dispersion Test

A simple screening test was used to determine the wetting behavior and the suspension stability of Si powder in the various liquids. The dispersion test was performed by introducing a small amount of silicon powder (100 mg) under glove box conditions into a glass bottle sealed with a thin rubber diaphram. Then, each of the liquids (15cc) was injected through the rubber stopper into the bottle with a syringe. This avoided introducing the liquids into the glove box. The mixture was lightly shaken and observed. All systems which incorporated the powder were subjected to an ultrasonic probe for three minutes to mix them thoroughly. After standing for 5 days, the suspensions were observed again. The results are discussed in the following section.

n-Propanol was selected for further testing based on the results of the mixing tests, contact angle measurements and its low surface tension. Samples were prepared using the following three methods.

• Hand mixing by shaking: A small amount of silicon powder (~ 1 mg) and n-proponol (10 ml) were mixed in a glass bottle in an N_2 atmosphere. The mixture was lightly shaken by hand and diluted to convenient concentrations for particle size measurements.

• Ultrasonic agitation: The powder suspensions were subjected to an ultrasonic probe to enhance wetting, dispersion, and fragmentation of agglomerates. While in a 25 ml beaker, the suspension was subjected to the ultrasonic probe* at 150 watts input power with a 1/2 inch diameter disruptor horn and 150 watts input power with a microtip. The suspension was cooled with a dry ice-propanol mixture during agitation. The effects of the ultrasonic treatment on the agglomerate size were examined by several techniques.

• Centrifugal separation of agglomerates: After mixing 500 mg of powder and 15 ml of n-propanol, the suspension was subjected to the ultrasonic probe for 3 minutes. The large agglomerates were removed by centrifugal separation at 12,000 rpm for 10 minutes. This removed approximately one half the powder. The Stokes' Law equivalent spherical diameter of the

---

* Heat Systems W225R

largest agglomerates still in suspension after this treatment is 260 nm. Then the supernatant of the first centrifuge was recentrifuged at 17,000 rpm for 2 hours. The supernatant of the second separation process contained very little powder but added a tan color to the dispersion. Particle size measurements were also made for this supernatant. The material cast from the second centrifuge was examined by SEM to determine its uniformity.

iii. Contact Angle Measurement

The contact angle formed by a sessile drop of representative liquids on single crystal silicon was measured to provide a basis for comparing the mixing test results of Table XII with surface properties of silicon. The silicon wafer, the surface of which was assumed to be initially oxidized, was cleaned in the following manner: after ultrasonic cleaning in trichloroethylene for 5 minutes, in acetone for 5 minutes, in methanol for 5 minutes and in distilled water for 5 minutes, the silicon wafer was put in a hydrofluoric solution (2.9 mol/l) for 5 minutes. The HF solution was then removed by successive dilutions with distilled water while blowing nitrogen into the solution until only distilled water remained. Under glove box conditions, the cleaned, etched and dried silicon wafer was immediately placed into a sealed chamber with an optical glass window and rubber stopper on the top, so that subsequent measurements were made in a nitrogen atmosphere.

After putting a drop (0.01 ml) of the liquid to be tested onto the wafer through the rubber stopper with a microsyringe, measurements were made at 23°C with an NRL Contact Angle Goniometer*.

b. Results of Dispersion Test

i. Screening Tests

Three types of behavior were observed during the dispersion tests (Table XII). These are:

• Good Dispersion (designated A): most of the particles remained well dispersed after several days. This phenomenon was observed for liquids with high dielectric constants such as aliphatic alcohol, benzyl alcohol, ketones and benzaldehyde.

• Poor Dispersion (designated B): most of the particles settled out of the suspension within one hour. This phenomenon was observed for liquids

---

* Model A-100, Rame-Hart, Inc.

TABLE XII

Results of the Dispersion Test and Contact Angle Measurements

		Dispersion Test Results	Contact Angle
Aliphatic Hydrocarbons			
1	n-Hexane	B	0°
2	Cyclohexane	B	*
3	n-Octane	B	0°
Benzene Group			
4	Benzene	B	0°
5	Toluene	B	0°
6	Xylene	B	*
Alcohols			
7	Methanol	A	0°
8	Ethanol	A	*
9	n-Propanol	A	0°
10	Isopropanol	A	*
11	n-Butanol	A	*
12	n-Heptanol	A	*
13	n-Octanol	A	0°
14	Benzyl Alcohol	A	14°
15	Ethylene Glycol	A	45°
Ketones			
16	Acetone	A	0°
17	2-Pentanone	A	0°
18	2-Heptanone	A	0°
Ether			
19	Isopentyl Ether	B	*
Aliphatic Acids			
20	Propionic Acid	B	0°
21	Butyric Acid	B	*
Aldehydes			
22	Benzaldehyde	A	6°
Inorganic			
23	Water	C	78°

A: good dispersion, no change and no precipitation after several days;
B: Poor Dispersion and settling; C: Flotation

*

Not Measured

with a very low dielectric constants such as n-hexane, cyclohexane, n-octane, benzene, toluene, xylene, isopentyl ether, propionic and butyric acid.

- Particle Flotation (designated C): all the silicon powder completely floated on the liquid surface. The particles could not be incorporated into the liquid even after vigorous agitation. This phenomenon was observed only for water. It is noteworthy that if the powder was exposed to air for several hours before mixing, it was easily wetted by water.

Among the good dispersing liquids (designated A) some are considered less desirable than others based on other properties. Methanol and acetone are very volatile. Butanol, heptanol, octanol, benzyl alcohol and ethylene glycol have high viscosities and consequently may be difficult to remove from the powder. Benzaldehyde is chemically unstable. n-Propanol was chosen for subsequent experiments since it generally has the most acceptable combination of properties and it has the lowest surface tension of the group.

ii. Contact Angle Measurements

Contact angle results are shown in Table XII. Zero values are found for liquids with surface tensions less than 30 mN/m. Non-zero values were measured for higher surface tension liquids like benzyl alcohol, ethylene glycol, benzaldehyde and water.

Our measured contact angle for water (78°) is smaller than that reported by Williams and Goodman[19] (85-88°), which was measured in pure water and an HF solution by the bubble method. The smaller value of the angle we measured is likely due to slight oxidation of the silicon wafer surface during handling in the glove box. Using the experimentally measured relationship between contact angles and oxide thickness reported by Williams and Goodman[19], 78° corresponds to 2-3 Å thick oxide layer. Since the atmosphere is controlled to less than 10 ppm oxygen in this experiment, this level of oxidation is considered possible.

iii. State of Agglomeration

The state of agglomeration of Si powder in n-propanol was evaluated by three techniques. These are:

- TEM – Specimens were prepared by dipping carbon coated TEM grids in suspensions of approximately 1 x 10^{-4} moles Si/liter. Excess suspension was removed by drawing off liquid with the edge of an absorbant paper.

61

Agglomerates of particles were spaced several hundred diameters apart on the grid so agglomeration during drying was not important. Results are shown in Table XIII.

- Laser Doppler particle size analysis - The state of agglomeration was measured by laser Doppler particle size analysis* and the results are given in Table XIII. This technique evaluates the equivalent particle diameter based on the velocity of Brownian motion. The diameters agree quite well with those determined by TEM. The dispersion factor is a qualitative measure of the width of the particle size distribution on a scale from 1 (narrow distribution) to 10 (wide distribution).

- Light scattering - Light scattering measurements were performed with a Universal Light Scattering Photometer**. The intensity of light scattered from the supernatant after the second centrifugation is shown in Figure 23 as a function of viewing angle. Theoretical curves calculated from Rayleigh scattering theory are placed in an arbitrary position on the figure since the concentrations needed for calculations were unknown. This theory is applicable for the case of particles that are uniform in size and are smaller than 1/20 of the wavelength of the light. For this case, the angular scattering profile for the vertically and horizontally polarized light differ since isotropic scattering polarizes the incident light. As shown in Figure 23, this causes the scattered intensity of the horizontal polarization to vary as $\cos^2 \theta$, while the vertical component is independent of scattering angle. Although there are deviations between the shapes of the theoretical and experimental curves, the Rayleigh scattering model represents the experimental curves quite well.

To insure that a single-particle rather than multiple-particle scattering occurs, measurements were also made as a function of the supernatant concentration. The intensity ratio (I_{90°/I_{0°) varied in a linear manner with concentration, indicating that single-particle scattering is dominant. For multiple-particle scattering at higher concentrations, intensity increases less rapidly.

---

* Coulter Electronics, Inc. Nanosizer
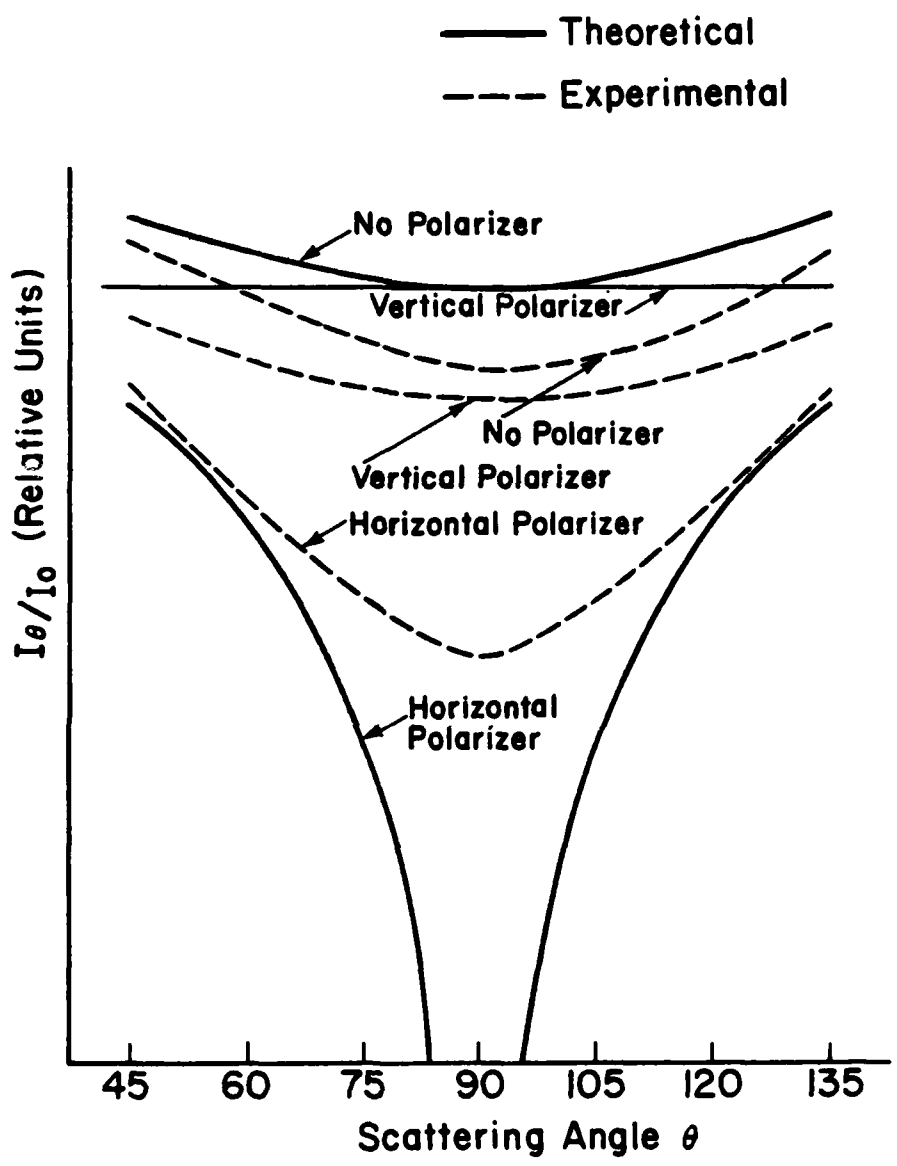**Brice Pheonix Inc.

Figure 23. Light scattering as a function of viewing angle for Rayleigh type scatterers.

TABLE XIII

State of Powder Agglomeration in n-Propanol Determined
by Several Techniques

	Light Scattering Analysis		TEM		Laser Doppler Analysis	
	Dissymetry Factor, Z	Corresponding Particle Diameter (Å)	Size (Å) Max.	Min.	Particle Diameter (Å)	Dispersion Factor
Suspension Mixed by Shaking	>2.5	–	6200	4400	8000	8
Suspension Subjected to Ultrasonic Disruption	2.67	–	4200	2000	2000	4
Supernatant from second Centrifugation	1.05	500	550	500	500	3

The agglomerate size can be determined by measurement of the dissymetry factor[20] provided the shape of the particle or agglomerate is known. This is given by:

$$Z_{45°} = \frac{\dfrac{I_{45°}}{I_{0°}} \text{ suspension} - \dfrac{I_{45°}}{I_{0°}} \text{ solvent}}{\dfrac{I_{135°}}{I_{0°}} \text{ suspension} - \dfrac{I_{135°}}{I_{0°}} \text{ solvent}}$$

where the I's are the light intensities measured at the indicated angles. This technique gives average aggregate sizes independent of particle refractive index, provided their shapes are known. It looses some accuracy at values of Z much larger than 2 since the values tend to be more dependent on chain stiffness, non-Gaussian chain branching, etc.[20] The dissymetry factor, Z, for the second supernatent (Table XIII) was calculated to be 1.05. Assuming a spherical shape, light scattering indicates a particle diameter of 500 Å. This result agrees with BET and TEM techniques. The supernatent of the suspension after the first centrifugation had a Z value of 1.83 indicating an equivalent spherical diameter of 1640 Å. This indicates agglomerates are made up of 2 or 3 particles. Values of Z near

2.5 were found for suspensions with a variety of larger agglomerate sizes as determined by TEM. Apparently the dissymetry factor Z becomes insensitive to size above $Z \cong 2.5$. Light scattering may be used to determine the sizes and shapes of larger agglomerates but requires the use of more complex analyses usually performed by a computer[21].

c. Discussion

The results of the dispersion tests were plotted with respect to the surface tension and dielectric constant of the liquids since these two parameters were found to be significant factors with respect to the wetting and dispersion of silicon. The results are given in Figure 24. Based on the contact angle results and the surface tension-dielectric constant diagram, wetting and dispersion properties of silicon are summarized as follows:

• Higher surface tension liquids (>30 mN/m, e.g. water, benzyldehyde, ethylene glycol, and benzyl alcohol) exhibited non-zero contact angles. However, particle flotation was only observed for water, which has an extremely high surface tension. The other three liquids, for which $\theta \neq 0$, did not float the powder. It is possible that the agglomerates were not fully wetted by the liquids, and thus these three may be less favorable than lower alcohols or ketones which exhibit a zero contact angle.

• Poor dispersion took place for liquids with a low dielectric constant, ($\kappa < 5$, e.g. aliphatic hydrocarbons, liquids of the benzene group, ether, and acids) for all values of surface tension. The absence of dispersion once the powder is wetted is directly related to the silicon-liquid surface tension and not to the liquid-vapor surface tension. These results suggest that poor dispersion occurs because of high liquid-solid surface tensions for these liquids.

• Liquids with high dielectric constants are concluded to be the ideal dispersing media. The surface tension of the liquid should be as low as possible to allow immersion and full penetration of the agglomerates by the liquid.

Analyses of the supernatants shows that the linear agglomerates observed in the Si powders can be broken up substantially. After centrifuging the ultrasonically treated dispersion, approximately one-half of the powder consisted of agglomerates consisting of 2-3 particles. This is a substantial improvement over the starting powders and should permit

65

70

60

50 Flocculated

Dispersed

40

30

20

10

Surface Tension (mN/m)

X23

Floated

•15

°22

•14

5
4 20
Δ 21
Δ 2
Δ 3
Δ 1

•13

11
16
9
17 10
•8

•7

A { • alcohols
    ∘ ketones
    ⊙ aldehydes

B { △ aliphatic hydrocarbons
    ▲ benzene group
    ▲ aliphatic acids

C x water

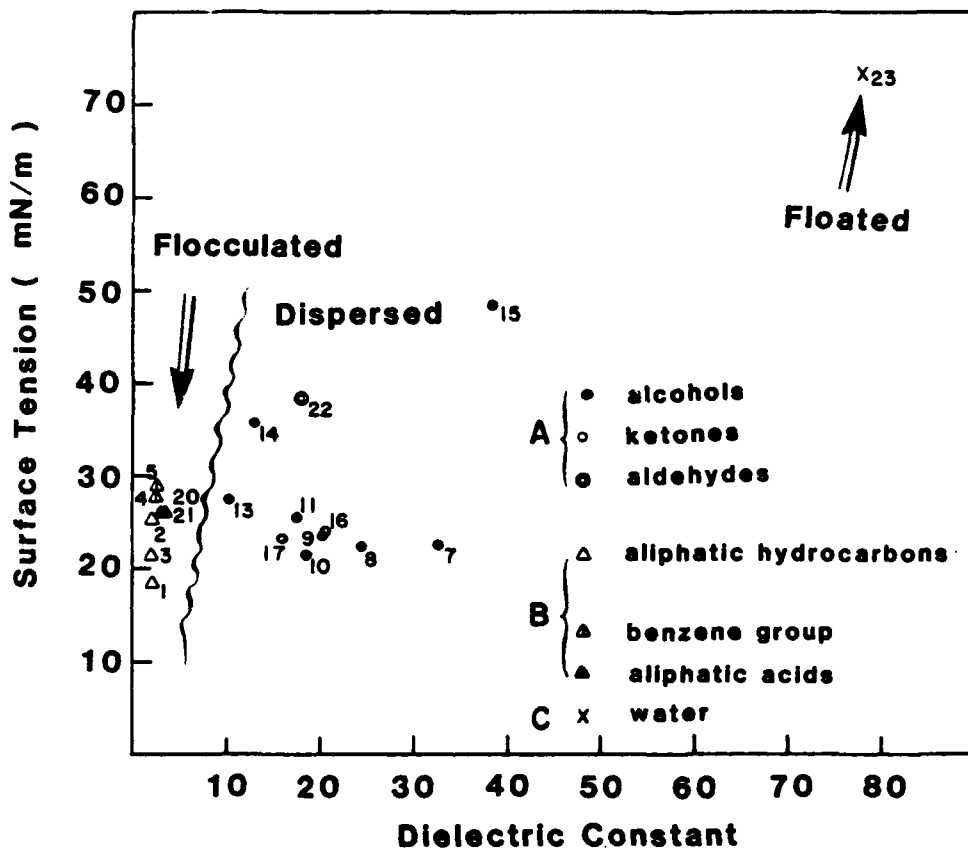10   20   30   40   50   60   70   80

Dielectric Constant

Figure 24. Correlation between dispersing characteristics and the liquid-vapor surface tensions and dielectric constants of solvents tested for forming stable dispersions of silicon powder.

slip and centrifugal casting processes to be used. Achievement of the ordered structures shown in Figure 1 requires complete dispersion.

In our interpretation, we have considered flotation and poor dispersion as separate phenomenon, however, each of these aspects of poor wetting is presumed to be related to a unifying phenomenon. If so, these two behaviors should be interpretable in terms of more suitable factors such as spreading coefficient, polarizability, or a more complex function of surface tension and dielectric constant. We are unable to develop this model at this time, thus, we have presented this data as an empirical observation (Figure 24). It does have considerable value in the selection of dispersing agents for silicon.

2. Sample Fabrication

a. Objectives and General Approach.

The development of powder processing techniques has been a major portion of our effort during this year. We have concentrated on handling procedures which avoid contamination, primarily by oxygen, and on techniques for packing powders that produce very uniform, dense compacts. The difficulties in producing sufficiently high density and, more important, uniformly dense green compacts are problems which are inherent to using fine powders. Both conventional and unconventional methods of shaping pieces made up of fine particles are being explored. Controlling the characteristics in the green state are extremely important, because defects in the green microstructures are not expected to be eliminated and may even be magnified during later processing steps. Two types of powder compacting have been used thus far: conventional uniaxial pressing, with subsequent isostatic pressing, and centrifugal casting. The equipment used for both the powder packing and sintering operations is set up within the glove box.

b. Experiments

i. Cold Pressing and Isostatic Pressing

This approach was used to make samples which permitted evaluation of sintering, nitriding and crystallization kinetics as well as strength and microstructural characterizations. It is recognized that it is difficult to achieve superior characteristics in pieces fabricated by these techniques because the powders are so fine. However, results did indicate that uniform densities and final void sizes less than $0.1 \mu m$ could be achieved, so these shaping techniques may prove technologically useful.

67

Pellets were cold pressed in the glove box at pressure levels up to 45,000 psi (single action die, diameter = 1/2 inch). Laminations resulted at these high pressures. It was found that the combination of cold pressing at lower pressures and isostatic pressing produced pellets with both adequate and uniform densities. Pellets were first cold pressed at 1000 psi and then isostatically pressed at 45,000 psi. After cold pressing, the pellets were sealed in double evacuated isopressing bags. All processing steps, except isostatic pressing, were carried out in the glove box.

These procedures yielded Si pellets with green densities between 0.95 to 1.15 g/cm^3 (40-49% of theoretical). The green densities of Si_3N_4 pellets were typically 1.1 g/cm^3 (35% of theoretical). As will be discussed in Sections III-B-3 through III-B-5, the resulting pellets densified and reacted uniformly to produce pieces having microstructural features with scales approaching those of the constituent powders.

ii. Centrifugal Casting

Casting of powders from suspensions offers the possibility of achieving very uniformly packed green compacts as well as very dense ones. Experimentally, monodispersed spherical powders in a sol have been settled to ordered structures much like FCC or BCC packing of atoms in a lattice[22,23]. The resultant density approaches 74% of the theoretical. These centrifugal casting experiments also provide an expedient means of evaluating the degree to which powders are dispersed.

To obtain dense, uniform compacts by casting as shown in Figure 1, it is necessary to achieve dispersions of non-agglomerated powders. Experimentally, first, the liquid must wet the powder, second, agglomerates must either be broken up or removed, and third, the powder must be uniformly dispersed in the liquid. These issues have been investigated and were discussed in Section III-B-1. Having achieved these dispersions, the powder must be either settled or slip cast to form a dense cake. For very fine powders, centrifugal casting is used to reduce the settling time to a reasonable value.

Several types of powder suspensions were centrifugally cast to permit the characteristics of the compact to be observed. Casting was performed in an IEC HT centrifuge capable of achieving a relative centrifual force (RCF) of 34,000 g's. Table XIV summarizes the Stokes' law time required to completely settle spherical particles in a 5 cm tube at the highest speed. The experimental settling times should be much longer since interparticle

68

TABLE XIV

Time Required to Completely Settle from 5 cm Deep Suspension of Water in a 34,000 g Field.

Diameter	Si	Si_3N_4
200 Å	86.5 min.	51.0 min.
400 Å	21.6 min.	12.8 min.
600 Å	9.6 min.	5.7 min.

interactions cause them to settle more slowly than predicted by simple Stokes' law calculations. The rate depends on the powder concentration and the double-layer thickness.

Several suspensions containing 0.5 g of powder per 10 ml of solvent were first settled for about one minute at a RCF of 17,000 g to eliminate the large agglomerates. A pellet was then cast from the supernatant at an RCF of 34,000 g. The second supernatant was then poured off. Unfortunately, all specimens so far have cracked to some extent during drying, even though they were dried very slowly.

One pellet cast from mixed silicon and silicon nitride powders in a water suspension was sufficiently large that a density measurement could be made. It was only 30% of theoretical density. TEM examination showed the particles did not achieve ordered stacking and it was even possible to see remnants of the agglomerate strings in the compact. These results corroborate the light scattering and laser Doppler analysis which indicated agglomerates persisted. More complete dispersion is required to achieve high densities.

The investigation of the casting phenomena will continue with concentration on two very important and presently unresolved problems: achieving a well-dispersed suspension having a high density of suspended powders, and drying the cast pellets without their cracking.

3. Si Sintering

This research program has considered densification processes in Si powders in conjunction with the work on reaction bonding. Typically, the center-to-center distances between particles do not change during the

69

nitriding reaction, so the final density is solely dependent on the green density of the starting silicon compact and the degree of reaction. Theoretically dense reaction-bonded silicon nitride cannot be obtained unless the initial compact density is approximately 1.93 g/cm^3 (85% theoretical density).

One of the drawbacks of using ultrafine silicon powder, such as that produced by the laser synthesis process, is the difficulty in forming a high density green compact. This results in a low nitrided density even if the piece nitrides to completion. For instance, the typically achieved green density of 1.04 g/cm^3 (45% theoretical) resulted in a fully nitrided piece having a density of 1.75 g/cm^3, which is only 55% of theoretical. To overcome this problem, we investigated techniques for densifying the fine silicon compact prior to nitriding.

Greskovich and Rosolowski[24] first reported that fine silicon powder compacts will sinter to near theoretical density at temperatures close to the melting point of silicon. They reported 1%, 2.5%, 8%, and 23% linear shrinkage for powders having specific surface areas of 1.9, 11, 14.6, and 55 m^2/g, respectively, for 1 hour cycles at 1350°C in an argon atmosphere. They concluded that densification will occur if the silicon powder is sufficiently fine (less than approximately 0.25 μm). Based on these results, it was concluded that the green silicon compacts could be pre-densified by sintering in Ar to a specific desired density level before they were nitrided. This procedure should eliminate the problem of low green density compacts.

Silicon powder synthesized from run 027S (Appendix II) was used in these initial sinterability experiments. This powder had a specific surface area of 67 m^2/g and an oxygen content of approximately 0.2% by weight. The powder was pressed into pellets using the techniques described in Section III-B-2-b. These pellets were sintered in an Ar atmosphere in a closed end alumina tube furnace. The samples (0.2 g weight, 1 cm diameter) were heated in a vacuum to 1100°C before introducing Ar and subjecting them to a specific sintering cycle.

The sintering conditions and results are listed in Table XV. These results indicate that the laser synthesized Si powder can be sintered to near theoretical density at 1350°C in one hour. This is consistent with the results of Greskovich and Rosowloski.[24] Fully dense silicon, however, is not expected to nitride completely since the closed porosity will inhibit

70

TABLE XV

Si Sintering Conditions and Results≠

Sample	Temp. (°C)	Time (min)	Initial Density* (g/cm^3)	Final Density (g/cm^3)	Surface Area (m^2/g)
027S-4	1350	60	1.07 (46%)	2.25 (96%)	**
027S-2	1350	0	1.01 (44%)	1.80 (77%)	5.92
027S-1	1250	0	1.06 (46%)	1.31 (56%)	25.4
027S-3	1250	10	1.03 (44%)	1.43 (61%)	17.5
027S-5	1250	10	1.00 (43%)	1.44 (63%)	**
027S-9	1250	20	1.00 (43%)	1.48 (64%)	14.6

≠ Powder lot 027S (surface area 67 m^2/g, 0.2% oxygen)
* Estimated densities
** Not measured

the transport of the nitriding gas. Table XV indicates that lower sintered densities can be obtained by using lower temperatures and/or shorter sintering times.

Surface area measurements were made on the sintered pellets. The results indicate that the porosity remains open as sintering proceeds. Also, a large surface area remains available in the partially sintered compacts, which is important for enhancing the nitriding kinetics.

Fracture surfaces of sintered Si compacts 027S-2 and 027S-3 were examined by the SEM. They revealed some very dense areas and some very porous areas, both areas several microns in size. Other regions of the fractured surface appeared to have a uniform microstructure with a typical feature size that approximates the particle size. These microstructures suggest that the inhomogeneities which were present in the green specimen were magnified by the sintering process. It is expected that it will be difficult to fully nitride the very dense regions, and even after full nitridation, the highly porous regions will have a density which is significantly lower than theoretical. Thus, it is very critical to achieve

a uniform microstructure in the pressed pellets. We are currently using conventional methods (cold pressing and isostatic pressing) and some more novel methods (centrifugal casting and electrophoresis) to produce these uniform green compacts (see Section III-B-2-b).

These experiments accomplished their major objective. It was demonstrated that the laser synthesized Si powders would densify without significant reduction in specific surface area. Also, the final density could be adjusted reproducibly from the level of the as-pressed pellet to nearly the theoretical value. Further work is required to improve the green microstructure of the Si pieces.

4. Si Nitriding

a. Objective

The three main factors which bring about the high strength of RBSN are a product that is 100% silicon nitride, a high fractional density, and a controlled microstructure, i.e. grain, flaw, and void sizes, with a controlled phase mixture. To retain its strength at high temperatures, the amount of glassy grain boundary phase must be kept to a minimum, requiring reasonable purity of the starting materials. Processing research has been initiated with the laser synthesized silicon powders to achieve these objectives.

The size of flaws in a ceramic body are usually related to the particle size of constituent powders, provided other classes of defects such as lamminations, dirt and exceptionally large grains, which result from discontinuous grain growth, have been eliminated. The smallest voids result from the interstices between particles which were not eliminated with heat treatment. Substantially larger voids result from clusters of agglomerated particles which can either enclose a void or cause particle rearrangements that leave a void. The smaller voids are approximately the same size as the particles and the bigger ones can be 10-100 times larger. It is important to control the particle size and, more important, the powder agglomerate size, since the fracture strength is inversely proportional to the flaw size. The silicon powders produced by the laser driven reactions would seem to be the ideal starting powders to produce such high strength silicon nitride due to their high purity, extremely fine particle size and shape. It still needs to be demonstrated that they are free of hard agglomerates. It would also be expected that the reaction rates for these powders would be much higher than those exhibited by conventional silicon

72

powders, thus allowing nitriding to completion at lower temperatures in shorter times.

To control the microstructure of the product, the nitriding kinetics must be controlled. At this point, a complete understanding of the nitriding reaction has not been gained. Although the literature contains many studies on nitriding kinetics,[25-29] there have been almost as many rate laws postulated as there have been experimenters.

A high final fractional density is dependent on achieveing a high fractional green density. Since the laser powders are so fine and have such a narrow particle size distribution, a pressed green density higher than 45% of the theoretical density of silicon is almost impossible to attain. This limits the final nitrided density to less than 60% of the theoretical density of silicon nitride. This low density can be over come by pre- or post-nitriding sintering or by using different processing techniques to produce a higher density green silicon sample.

b. Theoretical

There are several mechanisms of forming each of the two polymorphs as evidenced by the varied morphologies of silicon nitride produced[27]. The main mechanisms would seem to be a vapor phase reaction where $Si(g)$ or $SiO(g)$ reacts with N_2 to form the nitride which is deposited[27], and a condensed phase mechanism in which silicon (solid or liquid) reacts with adsorbed nitrogen to form the nitride in situ[27,30,31]. It is generally agreed the vapor phase mechanism forms α-silicon nitride, and is enhanced by lower temperatures, minor oxygen impurity levels, slow heating rates, and low gas flow rates, while the second mechanism forms β-silicon nitride and is enhanced by higher temperatures, Fe impurities, fast heating rates and high gas flow rates[26-29]. Although the oxygen and iron impurities are said to "enhance" the specific mechanisms, both impurities are considered undesirable. Oxygen, while enhancing the formation of the α phase in minute quantities, actually inhibits the reaction by formation of an amorphous SiO_2 layer around each grain when present in larger amounts. Iron enhances the formation of β-silicon nitride by forming a low melting $FeSi_x$ alloy, into which the β-silicon nitride will grow. Unfortunately, on occasion the molten alloy will flow into the voids surrounding neighboring grains, leaving a pore. Either the resulting large β crystal or the pore can be strength limiting defects[32], thus both Fe impurities and overheating should be avoided.

73

The steps which occur during the vapor phase reaction are as follows:

1) vaporization of Si from the surface of the particle
2) transport of the Si vapor in the gas
3) reaction of the Si with the nitrogen
4) transport of the silicon nitride in the gas
5) deposition of the silicon nitride onto the surface of the particle

In this sequence, the steps involving transport, (2 and 4), and vaporization of silicon (1) are not expected to be the rate limiting steps, thus, the reaction (3) or the deposition (5) step are expected to be rate limiting.

In the reaction between solid silicon and nitrogen gas the steps are:

1) adsorption of nitrogen onto the particle surface
2) transport of the nitrogen to the reaction sites via surface diffusion
3) reaction between the silicon and nitrogen.

In this mechanism, any of the three steps could be rate controlling.

For both of these mechanisms, each silicon particle will eventually become covered by a silicon nitride reaction layer. This would occur before all the silicon in the particle would have reacted to form the nitride, and additional mechanisms must be considered. In these, the steps would be determined by whether the silicon diffuses out or nitrogen diffuses in through the reaction layer. If the former, the steps would be:

1) transport of silicon through the reaction layer
2) reaction with nitrogen, either in the vapor or on the solid surface
3) if reaction in the vapor, deposition of silicon nitride onto the reaction layer.

If nitrogen diffuses in through the reaction layer, the steps would be:

1) adsorption of nitrogen onto the reaction layer
2) transport through the layer
3) reaction at the nitride-silicon interface.

The transport through the silicon nitride reaction layer, whether in or out, can be of two types: atomic diffusion or via microcracks. The transport rate through the microcracks is much higher than that via diffusion, resulting in a higher reaction rate.

Since the system of $3Si + 2N_2 \rightarrow Si_3N_4$ is so similar to the classical systems involving the oxidation of a metal, many of the models of the reaction postulated in the literature have been based on the oxidation models. These models include the familiar linear and parabolic rate laws [25,30,33,34] and those derived by Evans [35] for the oxidation of metals where transport is via microcracks. There seems to be experimental evidence for each model. This could be due to the many experimental techniques used: no two groups of researchers have used exactly the same equipment or procedures, and none achieved the same results.

Another type of transport must be considered in the nitriding reaction: the bulk transport of nitrogen gas into the powder compact. Since there is an approximate 22% volume increase associated with the reaction, porosity in the compact will be eliminated as the reaction proceeds if the initial silicon density is greater than about 75% of theoretical. Because of this, complete nitriding will be slow unless the pre-nitriding fractional density remains below 0.75. One would also expect the outer part of the compact to nitride before the inner, thus blocking off transport to the interior of the compact and preventing complete nitriding there.

The formation of silicon nitride is a highly exothermic reaction. If this is not taken into account during the reaction bonding process, problems can be encountered which range from catastrophic melting of the powder compact to localized melting of the silicon grains causing strength limiting voids. In general practice, these problems are avoided by slow, controlled heating of the compact to allow formation of a nitride layer around each silicon grain, after which the heating rate and final nitriding temperature can be increased. Careful consideration of the transfer of heat in the compact becomes of paramount importance, especially when working with very reactive powders. Since the heat produced is porportional to the amount of nitride produced, the rate of reaction as well as the mass of the compact needs to be considered in determining whether uncontrolled heating will occur.

c. Experimental Procedures

Although there is experimental evidence that certain mechanisms of nitride formation are enhanced by various "macroscopic" conditions, the mechanistic reasons for this enhancement on a "microscopic" level have not been determined. Only when these "microscopic" properties are understood

can the reaction kinetics be completely controlled. The general experimental strategy to this end would then be to determine the mechanisms and the rate controlling steps that are operating under various conditions. This requires a sensitive and controllable experimental system and a careful choice of the parameters to vary (since some of the rate controlling steps are sensitive to the same parameter), followed by complete characterization of the sample at every step.

The characterization techniques employed include particle size and grain size analysis (by BET, X-ray line broadening, SEM and TEM), impurity level analysis (by Auger, IR, wet chemistry and spectrographic techniques), and phase analysis (by X-ray) on the samples before and after nitriding. During the nitriding treatment, the temperature, change in weight and atmospheric conditions are monitored. Conventional metallography cannot be used with these exremely small physical features.

To determine the extent of reaction, two techniques are used: thermogravimetric and X-ray phase analysis. Each has its advantages and disadvantages. The thermogravimetric technique is easy to do during the nitriding experiment by simply measuring the changes in weight of the sample. This method gives no information on the phase composition of the product and may be of limited accuracy due to possible weight loss by silicon volatilization during the early parts of the heating cycle. X-ray phase analysis gives complete information on the relative amounts of α-silicon nitride, β-silicon nitride and Si present in the product and is not affected by silicon volatilization. No special equipment is needed, but many samples need to be analyzed to obtain complete information on the extent of reaction during the nitriding cycle. Also, the X-ray technique requires the construction of a calibration curve for highest accuracy.

d.   Nitriding Experiments

In the past year, four sets of nitriding experiments have been done; two sets using as-pressed pellets, and two sets using pre-sintered pellets. Each set was done for a different purpose, and thus was carried out in a different experimental environment. All samples consisted of pellets having the following nominal characteristics: 1 cm in diameter, 0.3 cm high, and 40-45% of theoretical density of silicon.

The first set of experiments consisted of preliminary nitriding runs to determine if the laser powders would indeed nitride and whether the reaction

rates for these powders differed from those of conventional powders. This first set of experiments were carried out in an Al_2O_3 muffle tube furnace in a static N_2-5% H_2 atmosphere at 2 psig. The samples were heated under vacuum to 1100°C since they were exposed to air during loading into the furnace. The heating rate was approximately 250°C per hour. Two lots of laser powder were used in these experiments, 215S and 216S (see Appendix II for the powder characteristics). Although the surface areas were different, the powders nitrided similarly (Table XVI). The major conclusion derived from the first set of experiments is that these powders will nitride and they are much more reactive than conventional silicon powders. Several other conclusions can be drawn from these results:

1) Silicon does not react with nitrogen appreciably at 1200°C in one hour, but does at 1316°C (216S-A & 216S-E)

2) The majority of nitride formation is completed in less than one hour at 1316°C (216S-E & 216S-C)

3) Complete nitriding is possible by heating the mostly nitrided pellet to 1625°C, well above the melting point of silicon, for short times, with no appreciable changes in the microstructure, surface area, phase composition or crystallite size. (216S-J & 216S-C)

4) Near complete nitriding can be achieved by a low temperature, long time heating cycle, with about the same amount of coarsening as in the rapid cycle, although the microstructure is more uniform. (216S-B & 216S-J)

Microstructural examination (SEM) has been performed on 215S-B, 216S-A, and 216S-E. After heating a Si compact to 1200°C for 1 hour (216S-A), there was no reaction and no discernable change in microstructure over the green Si compact. Sample 215S-B, which reacted to 97%, had much the same microstructural features as the starting Si compact, i.e. small, uniform, and spherical grains. In contrast, a large microstructural change was observed for 216S-E (1 hr at 1300°C) which reacted to 74%. This sample consisted of high density regions 3-5 µm in size, interspersed with low density regions 1-2 µm in size. It appears that slower heating rates and longer times at lower temperatures yield superior microstructures.

The second set of experiments comprised a kinetic study[36]. For this group, thermogravimetric measurements were performed in the glove box using

TABLE XVI

Nitriding Histories and Resulting Characteristics

Sample	Green Density (g/cm³)	Heat Treatment	% Nitrided	Nitrided Density (g/cm³)	Nitrided BET Surface Area (m²/g)	Nitrided Equivalent Spherical Diameter (Å)	X-ray Phase Composition Si/α/β (Wt %)	Crystallite Size, X-ray Line Broadening Si/α/β (Å)
215-S-B	-	1082°C 16 hrs 1227°C 45 hrs 1330°C 24 hrs	97	-	18	1415	3/81/17	-
216-S-D	1.12	-	-	-	28.5	903	100/-/-	100/-/-
216-S-A	1.09	1200°C 1 hr	0	1.08	(pellet) 32.5	792	100/-/-	123/-/-
216-S-E	0.95	1316°C 1 hr	74	1.39	8.3	2431	26/60/15	443/271/273
216-S-C	1.09	1316°C 4 hrs	79	1.67	7.7	2583	21/63/16	300/260/460
216-S-J	1.03	1316°C 4 hrs 1625°C 0.5 hr	100	1.68	9.0	2083	-/80/20	-/300/490

a tungsten induction furnace. Since the glove box was used, the atmosphere was static nitrogen rather than the N_2-5%H_2 mixture used in the first set of experiments. The temperature was increased rapidly to 1020°C, and held for 5 minutes to allow the system to equilibrate, then the temperature was increased rapidly to the nitriding temperature. The first weight measurement was made 2 minutes after the nitriding temperature was reached and was considered the zero point. Only one powder lot (103S) was used in this set of experiments which was intended to determine the effect of temperature on the reaction rate.

This set of experiments produced the four curves shown in Figure 25 for the fractional weight gain vs. time at 1275°, 1300°, 1325°, 1400°C. At the three lowest temperatures the curves exhibited two distinct regions; a linear region, followed by a second region best described by the asymptotic rate law derived by Evans[35]. The initial reaction rate in the asymptotic region is about 10 times that of the linear region. In the second region the slope goes to zero indicating that no further nitriding takes place. The highest temperature studied did not exhibit the initial linear region.

Comparison of these results with others in the literature brings out two important points:

1) The laser synthesized silicon powders are much more reactive than conventional silicon powders, nitriding to the same extent in much shorter times[25,29]. This agrees with the conclusion from the first set of experiments.

2) In contrast to conventional silicon powders, as the nitriding temperature is increased the total extent of reaction decreases[25,30]. At short times this anomaly is masked by the linear region where the nitriding rate increases with increasing temperature. This phenomenon has not yet been explained.

The information required to complete the heat transfer analysis as discussed earlier can be obtained from these reaction rate curves. Each curve can be approximated by two linear regions, and the rate of formation of the nitride, dn/dt, can be calculated for each. This value, combined with the heat of formation, ΔH_f, at that particular temperature, can be used to find the rate of heat production in the compact using

$$\dot{Q} = \left| \Delta H_f \right| dn/dt$$
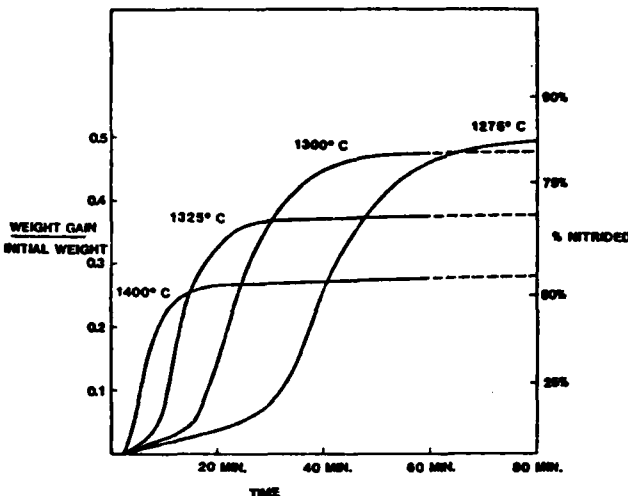
Figure 25.   Fractional weight gain as a function of nitriding time at
               various temperatures.   The % nitrided scale was calculated from
               the weight gain.

where $\overset{\bullet}{Q}$ is constant for each linear region. The difference in temperature
between the center and the surface of a cylindrical shape is given by[37]:

$$\Delta T = \frac{SR^2}{4k}$$

where S is the rate of heat production per unit volume, R is the radius of
the compact, and k is the effective thermal conductivity.

Heat transfer should not be a problem for any of the temperatures in
the first linear region. The largest calculated temperature increase is
2.7°C for the 1325°C reaction rate. In the second linear region at the
highest temperature, 1400°C, the calculations indicate that the temperature
at the center line is over 21°C higher than the surface of the pellet, thus
bringing the interior to almost 12°C above the melting point of silicon.
Catastrophic melting of the pellet did not occur. The absence of melting
could be explained because these calculations were based on the geometry of
an infinite cylinder and thus the heat loss from the ends was ignored.
Also, they assume that the reaction proceeds uniformly throughout the volume
of the sample. The surface reaction may have slowed the interior reaction
by depriving it of nitrogen. Taken in total, the results of these
calculations indicate that for small samples, heat transfer should not be a

problem in terms of catastrophic melting, although localized melting of individual grains of silicon may occur. For larger samples, this analysis can guide the selection of the best nitriding temperature and rate to avoid overheating.

The heat transfer calculations also imply that the change of the reaction rate from a linear to an asymptotic behavior cannot be attributed to runaway heating of the pellets.

Two different types of nitriding studies were performed on silicon pellets which had been pre-sintered in Ar. In one, the silicon was sintered in Ar, removed from the furnace, analyzed and returned to the furnace for nitriding. In the second case, silicon samples were sintered in Ar and then the atmosphere was changed to N_2 - 5% H_2 for nitriding. It was found to be beneficial to pull a vacuum for a half hour at 1100°C between the sintering and nitriding steps to remove the Ar from the porous sample and permit the nitrogen mixture to enter.

A comparison of the results shown in Table XVII indicates that both Ar-sintered and non-sintered samples exhibited the same general nitriding characteristics. Pre-sintering yielded pieces with densities comparable to the highest density RBSN from other sources.

Samples which were sintered and nitrided without removing from the furnace, nitrided less completely than samples which were pre-sintered, removed from the furnace and analysed, and then returned to the furnace for the nitriding cycle. This is observed by comparing samples 027S-5 and 027S-9 (Table XVII) with samples 027S-8 and 027S-10, whic. were all subjected to similar sintering and nitriding cycles, and may have resulted from achieving higher sintered densities in the sequential process. The estimate of shrinkage during sintering assumed that no dimensional changes took place during nitriding. Comparison of 027S-8 (a sequential sintering-nitriding run) and 216S-E (a sample not pre-sintered in Ar) indicates that the degree of nitriding was more complete in the sample which was not pre-sintered. This may be related to the inability of nitrogen to enter a more dense specimen during a short nitriding cycle.

Microstructural examination of fracture surfaces by SEM of sample 027S-5 did not reveal either the high density regions or the very porous regions which had been seen in the fracture surfaces of Ar-sintered silicon specimens 027S-2 and 027S-3. This sample also nitrided to near completion,

81

TABLE XVII

Nitriding Histories and Results for Presintered Pellets

Sample	Green Density (g/cm³)	Heat Treatment	% Nitrided	Nitrided Density (g/cm³)	Nitrided BET Surface Area (m²/g)	Nitrided Equivalent Spherical Diameter (Å)	X-ray Phase Composition Si/α/β (Wt %)	Crystallite Size, X-ray Line Broadening Si/α/β (Å)
Presintered in Ar		(See Table XV)						
027S-5	1.44*	1250°C 48 hrs 1350°C 24 hrs	97	2.34	7.7	2450	3/66/31	-/370/580
027S-9	1.48*	1250°C 48 hrs 1350°C 24 hrs	97	2.52	7.5	2520	3/67/29	-/650/750

Sample			% Nitrided	Nitrided Density (g/cm³)			X-ray Phase Composition Si/α/β (Wt %)	Est. Si Density
Sequential Sintering and Nitriding								
027S-8		See Below	63	1.87	--	--	63/27/10	1.60 (69%)
027S-10		See Below	88	2.74	--	--	12/60/28	1.78 (77%)

	in Ar		in N₂-5% H₂	
Sample	Temp.	Time	Temp.	Time
027S-8	1250	10	1300	1 hr**
027S-10	1250	10	1250	72 hr**
			1350	24 hr**

* Ar sintered density
** A vacuum was pulled for 1/2 hour between Ar and N_2 - 5% H_2 anneals.

as shown in Table XVII. Polished surfaces were examined by optical microscopy to determine whether unreacted silicon was visible. Unreacted silicon shows up as highly reflective areas by optical microscopy. No such areas were seen, so it was concluded there were none greater than 1 μm in size.

The polished surface also permitted the size of the flaws to be estimated. Approximately 1 - 5 μm diameter voids could be found throughout the surface. These voids, which probably result from agglomerates, must be reduced in size to improve the brittle fracture strength. The next smallest group of flaws were approximately 1000 Å to 2000 Å pores. The 1-5 μm voids are much smaller than voids observed in reaction bonded silicon nitride made from conventional powders[38]. The void size in parts made from laser synthesized silicon powders can probably be greatly decreased by improved dispersing and shaping techniques.

The nitriding experiments performed so far with laser synthesized powders have indicated that it is possible to nitride these powders to completion and to achieve fine microstructural features via nitriding schedules involving lower temperatures and shorter times than the schedules used for conventional silicon powders. A high fractional final density of the nitride product is the desirable property that has been elusive throughout this year. This has resulted from the low green densities characteristically obtained with these fine Si powders.

The pre-sintering nitriding procedure has been demonstrated to be a viable way of producing high density RBSN. The combined pre-sintering and nitriding cycles must be further studied to define the optimum process. It appears likely that a high density RBSN can be produced by this procedure which will have strengths comparable to silicon nitride produced by the more expensive hot pressing technique.

Next year, the nitriding experiments, to be performed in conjunction with the sintering studies, will be directed at the determination of the properties which most affect the nitriding process and the characteristics of the samples. This will entail complete characterization of each powder lot at every step of the process, from pressing to post-nitriding. These characteristics combined with kinetic studies should provide a basis for interpreting the physical and chemical phenomena.

5. Silicon Nitride Sintering

a. Objective

To date, stoichiometric Si_3N_4 has not been densified without resorting to sintering aids, applied pressure or both.[39] This is due to the sintering being dominated by mechanisms which cause neck growth without reducing interparticle distances. The relative rates of the mass transport processes are particle size dependent and it has been proposed[24] that processes which cause densification may dominate the sintering process if the Si_3N_4 particles are made sufficiently small.

This program has investigated the feasibility of densifying the laser synthesized Si_3N_4 powders without additives or pressure. It is important to eliminate the additives used for sintering aids because they degrade high temperature mechanical properties, and it is difficult to produce intricate shapes by the more expensive hot pressing technique. Substituting simple sintering processes reduces manufacturing costs and permits much more complex shapes to be fabricated.

b. Background

Sintering is traditionally separated into three stages: initial, intermediate and final. In the initial stage, interparticle necks form and grow, in the intermediate stage, porosity changes from interlinked to discrete, and in the final stage, the remaining isolated pores are eliminated. Mass transport mechanisms which operate during sintering can be divided into those which cause densification (lattice and grain boundary diffusion and viscous flow) and those which cause only coarsening of the structure (evaporation-condensation and surface diffusion). The identities of the dominant transport mechanisms during initial stage sintering are usually inferred from neck growth rates, surface area changes and shrinkage rates under isothermal conditions. Sintering models for the latter two stages concentrate on the effects of grain and pore size distributions as well as surface area changes. The scale of microstructural features often change during the latter stages of sintering[40] which can cause a change in rate controlling mechanisms.

Pure silicon nitride is highly covalent (70%), and for a long time was classified as unsinterable because the Si and N diffusivities are so low. Silicon nitride is presently densified with the addition of oxide sintering aids. These react with the Si_3N_4 and the silica on the surface of the Si_3N_4

particles to form a liquid phase during heat treatment.[41] Densification takes place by rearrangement followed by a solution-reprecipitation mechanism.[42] Typical sintering aids include $MgO(3-5\%)$, Y_2O_3 (4-15%) or combinations such as BeO (1-2%) + MgO (3-4%).[39] Parts produced in this manner have sintered densities in the range of 85-97% of theoretical. Weight losses due to the dissociation of silicon nitride are typically 4-15% which resulted in some research being done using high nitrogen pressures to suppress decomposition.[43] The high temperature performace of the sintered nitrides is limited by the presence of glassy secondary phases at the grain boundaries which result in high creep values, and limit fracture strengths.

It has been shown[24] that there is no fundamental thermodynamic barrier to the densification of Si_3N_4 and that the final microstructure is determined by the operative mass transport mechanisms. It has been proposed[24] that the ratio of diffusivity to particle size should be on the order of 10^{-6} cm/sec for densification processes to dominate in covalently bonded solids. Based on this criteria and a diffusivity of 5×10^{-12} cm^2/sec (for nitrogen in Si_3N_4 grain boundaries at 1800°C)[41], densification should be observed with particle sizes less than 500 Å (38 m^2/g surface area). This maximum diameter is larger than is typically produced by the laser synthesis process.

In addition to having a small particle size, the laser synthesized powders are amorphous and can contain excess Si. The excess Si is known to lower the crystallization temperature of amorphous Si_3N_4 relative to the 1490°C measured[45] for stochiometric Si_3N_4. It will also nitride during the sintering heat treatment and thus will contribute a microstructural characteristic which is distinct from that originating by a sintering process. Both the nitriding and the crystallization processes have moderately high driving forces associated with them which may contribute to the densification process. For instance, the amorphous to crystalline transformation has been reported to cause an increase in the shrinkage rate during hot pressing[45,46]. Similar results might be expected in sintering without resorting to applied pressure.

c. Experiments and Results

Two sets of sintering experiments were undertaken. The sintering temperature was varied in one (A and B series) and was held constant in the other. The process conditions and powder characteristics are summarized
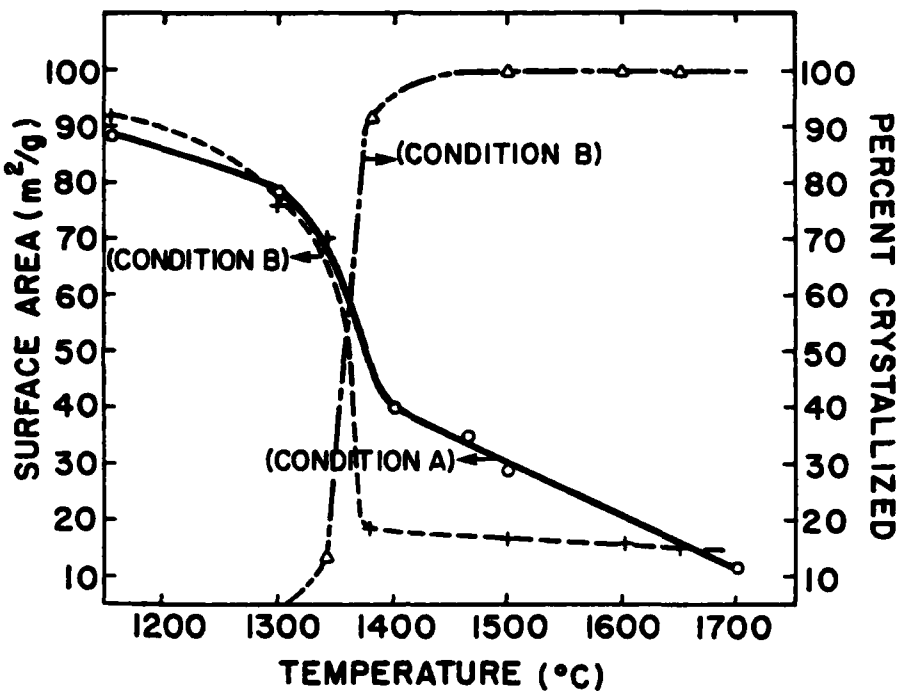
Figure 26. Percent crystallized and surface area as a function of Si_3N_4 sintering temperature under conditions A and B.

Table XVIII. The results of the experiments are given in Tables XIX and XX and in Figure 26.

SEM micrographs of samples sintered for 30 minutes at 1650°C showed that the constituent particles were in the range of 700-1400 Å. This dimension is consistent with BET surface area measurements and TEM microscopy. In this case particle size had increased substantially beyond that of the as-synthesized powders (~ 200 Å). The partially crystalline samples showed a bimodal particle size distribution. Regions, about 7500 Å in size, which had pulled away from the surrounding matrix, contained individual particles 500 - 1000 Å in diameter that had an aspect ratio of 2/1. The remaining regions were made up of 200 - 400 Å particles that had an aspect ratio of 1; these appeared much like the as-pressed particles. Resolution was not sufficient to determine whether interparticle necks had formed between the smaller particles.

TABLE XVIII

Powder Characteristics and Processing Conditions used for Sintering Si_3N_4

Firing Condition	Powder Lot	Cold Pressed (psi)	Isostatically Pressed (psi)	Green Density (% Theo.)	Furnace	Nitrogen Pressure (atm)	Sintering Time (min)	% Excess Si
A	021SN	5000	45,000	40	*	1.5	60	15
B	402SN	5000	no	20	**	1.0	30	17

* Al_2O_3 muffle resistance
** Tungsten induction

TABLE XIX

Results of Variable Temperature Sintering Si_3N_4

Temp. (°C)	Firing Condition	Phases Present				BET Equivalent Diameter (Å)	Crystallite Size *** (Å)		SEM Size (Å)
		%α	%β	%Si	%Amor.		α	β	
Room	A	0	0	0	100	200	–	–	–
1300	A	0	0	0	000	240	–	–	–
1400	A	87	8	5	*	457	294	–	400
1480	A	89	11	0	*	535	313	–	–
1500	A	81	19	0	*	692	323	–	–
1700	A	7	93	0	*	1550	473	–	Plates 1 μm
Room	B	0	0	0	100	204	–	–	–
1300	B	4	0	0	96	247	–	–	–
1340	B	14	0	0	86	265	403	–	≠
1380	B	53	38	0	8	1045	469	280	≠≠
1500	B	60	40	0	0	1106	374	339	–
1600	B	60	40	0	0	1176	440	346	–
1680	B	58	42	0	0	1254	678	662	≠≠≠
1680**	B	43	57	0	0	1880	>1000	607	–

* These are ratios of α/β/Si, no determination of % amorphous was made.
** This sample was sintered 1 hr.
*** By X-ray line broadening.
≠ Two size ranges: 200–400 Å, aspect ratio ~ 1/1
                    500 x 1000 Å, aspect ratio 1/2
≠≠ 800 x 1600 Å, aspect ratio 1/2
≠≠≠ 1000 x 2000 Å, aspect ratio 1/2

d. Discussion

The results given in Tables XIX and XX and in Figure 26 provide a phenomenological descripton of the powders' response to a sintering heat treatment. They are not sufficiently complete to be used as a basis for a mechanistic analysis.

Heating to temperatures in excess of 1300–1400°C causes an abrupt decrease in specific surface area that is accompanied by the emergence of

TABLE XX

Results of Isothermal Sintering of Si_3N_4 (B Conditions)

Temp. (°C)	Time (min)	X-ray Phase Analysis				BET Diameters (Å)	Crystallite Size by X-ray Line Broadening (Å)
		%α	%β	%Si	%Amor.		
1340	30	14	0	0	86	265	403
1340	60	21	0	0	79	300	452
1340	90	33	0	0	67	330	569
1340	120	42	0	0	58	482	260

crystalline Si_3N_4. This indicates that sintering models cannot be applied to processes which include exposure to temperatures in excess of 1400°C because these models do not include the effect of phase transformations. The results in Table XX indicate that from the time when changes first become evident, the diameters of the emerging crystalline particles exceed the diameters of the original amorphous particles. This result may indicate that the amorphous particles coalesced into groupings of particles prior to the onset of crystallization. Alternatively, the crystallization process may have caused the change in scale.

Two size ranges of particles were observed by SEM in the partially transformed samples. The diameters of the small particles are close to those of the originally amorphous powders. The physical diameters of the larger particles (500-1000 Å, aspect ratio ~ 2/1) agreed closely with the crystallite diameters as determined by X-ray line broadening. With increasing sintering temperature, the BET spherical equivalent diameters progressively agree more closely with the crystallite diameters. It has not yet been determined conclusively whether there is an exact correlation between particle size and crystallinity as would be done by TEM characterization, but it appears likely that the smaller particles are amorphous and the larger particles are crystalline.

The cause of the two particle size ranges observed by SEM for partially transformed samples is speculative at this point. If inhomogeneities exist in the distribution of the excess Si, they could cause some areas to sinter and/or crystallize faster than others. SEM micrographs and surface area measurements indicate that the larger particles in the partially transformed samples are either fully dense, or if they contain residual porosity, it is isolated from the surface. If the dominant mass transport mechanism was one which caused densification and pore closure on a local scale, the fact that certain areas sintered much faster and pulled away from the surrounding matrix could explain why no macroscopic shrinkage was observed. The dominance by a mass transport mechanism that causes only coarsening could result in these low surface area regions, if the mechanisms in fact can cause pore closure in low density compacts. This issue is unclear in simple systems and is particularly obscure in this material that involves a crystallization process and a stoichiometry that is potentially spatially variant.

The change of scale which accompanies crystallization requires mass transport, but it does not need to include the entire volume of the crystalline particles. The transformation could occur by a phase boundary, which originates from a single nucleation point, passing through contacting particles that were originally amorphous. In this case, the "crystallite size" would be multiple particle diameters. The decrease in specific surface area requires that porosity included within these groupings of particles having the same crystallographic orientation become isolated from the surface. This latter process may be a conventional sintering process which may or may not cause densification.

The crystallization process is also complex. The α-Si_3N_4 forms directly from the amorphous phase and, with extreme heat treatment, will transform to β-Si_3N_4. It also appears that by its sudden appearance at lower temperatures, β-Si_3N_4 emerges directly without going through the polymorphic transformation. The role of the excess Si is unclear. In the A series, it emerged as crystalline Si which was then consumed by nitriding. It did not emerge as a crystalline phase in the B series.

It is evident that sintering these powders is complicated by the simultaneous crystallization and nitriding processes. Achieving high green densities is important for improving the likelihood of achieving

densification. This will be approached by the dispersion techniques used with the Si powders (Section III-B-1) as well as conventional powder processes. The use of stoichiometric powders will simplify interpretation in future experiments. This work will be pursued since it represents such an important opportunity to make substantial improvements in the high temperature mechanical properties of Si_3N_4.

IV SUMMARY

This research program has investigated the means of producing Si, Si_3N_4 and SiC powders with special characteristics as well as means of fabricating these materials into ceramic bodies which exhibit superior characteristics. The powders which are sought will permit major changes in powder processing techniques and improvements in the defect structures of these brittle materials. Ideally, it should be possible to create green bodies of these materials having a close-packed ordered arrangement of the constituent particles (Figure 1) as has been done with metallic and oxide dispersed systems. These bodies will exhibit a minimum uniform shrinkage with sintering. Flaw sizes should approximately equal the diameters of constituant particles. Coordination numbers should be high, which will virtually eliminate rearrangement and will enhance densification processes. Even if the ordered structures are not achieved, it should be possible to attain most of the anticipated advantages in random structures.

Ideal powders will have particles which are small, uniform in size, equiaxed (tending toward spheres) in shape, composed of a specific phase(s), compositionally pure and free of agglomerations. In principle, gas phase synthesis processes can achieve these attributes, however, variations in time-temperature history throughout the conventionally heated reaction zones cause unacceptably large variations in particle characteristics. Also, the typically long exposure to elevated temperatures causes particles to bond to one another. We have elected to heat the reactant gases by absorbed IR light emitted from a laser. This unique means of transferring energy to the gas permits precise, uniform heating with unusually high heating rates and small reaction volumes. We anticipated that this laser heated synthesis process would overcome the deficiencies of conventional gas phase synthesis processes, while retaining their advantages.

In this process, optically absorbing gases are passed through a laser beam to cause a reaction within the region where the two intersect. We have investigated process geometries in which the gas stream and the laser beam intersect orthogonally and also where they intersect coaxially from opposite directions (counter flow). A CO_2 laser was used as the heat source to drive the reactions in gases containing active components such as SiH_4, NH_3, CH_4 and C_2H_2 as well as inert dilutants. The resulting Si, Si_3N_4 and SiC

powders were collected and characterized as a function of process variables.

The results of this research program demonstrate that this laser heated synthesis process produces powders with virtually all of the desired characteristics. The resulting particles are small, uniform in size, spherical and pure. The particles appear to be attached to one another in chain-like agglomerates, although direct examination by TEM revealed no neck formation between the particles of the Si_3N_4 and SiC powders. We anticipate that they can be dispersed. It has not been determined whether the necks observed between Si particles result from elastic deformation or from sintering, but it was demonstrated that a large fraction of them could be dispersed completely. Besides producing powders with ideal characteristics, this laser heated synthesis process is extremely efficient. Approximately 95% of SiH_4 is converted to Si or Si_3N_4 powder in a single pass through the laser beam. Also Si, Si_3N_4, and SiC powders can be produced from these reactants with as little as 2 kWhr of energy per kilogram of powder. It is likely that this process can produce both a superior and lower cost powder than conventional gas phase or solid phase synthesis processes.

Much of our efforts have focused on developing an analytical description of the laser heated synthesis process. To develop a model, many fundamental property measurements were required, such as detailed absorptivity measurements for reactant gases as a function of pressure and emitted wavelength. Emissions from the reaction have been studied to identify reaction species and to estimate the reaction temperature. Computer analysis of the gas flow were used to predict gas stream dimensions and velocities. Combined with direct observations of both the reaction positions relative to the laser beam and the reaction temperatures, these analyses and characterizations have been used to describe the time-temperature history of the reactant gases throughout the course of the reaction.

With the process conditions used for the majority of these synthesis experiments (laser intensity = 765 watts/cm^2, pressure = 0.2 atm, gas velocity = 500 cm/sec), reaction products were evident within 3-5 mm penetration into the laser beam. Heating rates to the reaction temperature (approximately 1000°C) were approximately 10^6°C/sec. The reaction was initiated in approximately 10^{-3} seconds and was completed in, at most,

7.5×10^{-3} seconds. The individual particles grew from and depleted a volume of gas equal to a sphere approximately 1×10^{-4} cm in diameter.

Most process variables were manipulated to determine their effect on particle characteristics. These interactions were interpreted in terms of changes in the process. Laser intensities up to 10^5 watts/cm^2 produced heating rates in excess of $10^{8°}$C/sec. Variations in heating rates within different gas stream were analyzed in terms of the Gaussian intensity in the laser beam and the parabolic velocity profile in the stream. The effects of nonabsorbing gases were also considered. Other than laser intensity and gas pressure, most process variables had very little effect on particle size. The gas depletion volume remained essentially constant. Increased laser intensity caused the reaction temperature to increase and caused the particle size of the Si_3N_4 particles to decrease and the size of the Si particles to increase. The relative temperature coefficients for the nucleation and growth processes exhibited by these two reactions are different from one another.

The general characteristics of the powders of the three materials are similar to one another, but they differ in detail. Silicon powders were crystalline under all but the lowest laser intensity conditions. Individual crystalline particles consisted of multiple grains which were approximately 150 Å in diameter. Mean Si particle diameters were in the range of 500-600 Å with a standard deviation of 35-50%. Silicon nitride powders were always amorphous. Mean particle sizes ranged from 25-220 Å, depending primarily on the laser intensity. These powders were more uniform than the silicon powders. The standard deviations were approximately 25% and the ratio between the largest to the smallest observed particle was less than 2.5. The stoichiometry varied with processing conditions. High laser intensities yielded stoichiometric powders; lower intensities produced powders which were rich in silicon. The silicon carbide powders are similar to the Si_3N_4 powders, (amorphous and tending to be rich in silicon), with a mean particle size of approximately 230-250 Å. Powders of all three materials are comprised of spherical particles whose BET equivalent diameters equaled the directly observed mean diameters. This observation and direct density measurements indicate that individual particles contain no porosity. All of the materials were free of contaminants. The oxygen impurity level decreased progressively as handling procedures improved. In

later powder batches, the O_2 content was less than 0.05% by weight. Levels of other impurities detected by emission spectroscopy generally totaled less than 100 ppm.

Resulting powders have been processed into pellets in the controlled atmosphere of the glove box. Silicon powders were nitrided and silicon nitride powders were sintered without sintering aids. The results of the nitriding experiments were particularly important. Silicon powders were nitrided to completion in the form of pellets whose densities could be controlled by a pre-nitriding sintering step. Relatively rapid reaction rates were observed because of the small particle size, but no problems were encountered with thermal runaway. The grain size and interparticle pore size in the resulting pieces were less than 1000 Å. The larger pores ($\sim$ 1-5 µm) probably resulted from agglomerates and can therefore be eliminated with adequate dispersion. The results of the Si_3N_4 sintering experiments are open to interpretation. There is evidence that densification occurred on a local scale without the use of sintering aids. If true, this has important consequences for improving high temperature mechanical properties.

A systematic study of developing stable dispersions was undertaken. n-Propanol was the best organic liquid studied. Pieces were centrifugally cast from these dispersions.

This research program has easily achieved its primary objective. Powders which result from the laser heated, gas phase synthesis process have most of the characteristics presumed to be ideal for ceramic powders. Also, the resulting powders can be processed into high quality pieces. The process also appears capable of reducing the cost of these powders because it requires very little energy per kilogram of powder and utilizes feed materials very efficiently. It still needs to be developed further to eliminate the tendency to form chain-like agglomerates and to increase the mean particle size. For many materials, it is desirable to have mean particle sizes of approximately 1000 Å rather than 250 Å as typically produced by this process. Achieving a larger particle size will require an improved understanding of the nucleation and growth processes. It is also important to apply the process to other materials. Many electronic, magnetic, and optical ceramic processes would benefit from using powders with the characteristics demonstrated in this research program.

Appendix I

	Laser Inten-sity (W/cm^2)	Cell Pressure (atm)	SiH$_4$ ($\frac{cm^3}{min}$)	NH$_3$ ($\frac{cm^3}{min}$)	Ar †† ($\frac{cm^3}{min}$)	Ar †† ($\frac{cm^3}{min}$)	Max. Gas Velocity at Nozzle (cm/sec)	Reaction Zone Temp. by Pyrometer (°C)	Filter (g)	Total in Cell +Filter (g)	Total Eff. (%)
Lot #				Run Conditions						Wt. Collected	
215S	760	0.2	11	0	0	1000	104	*	*	2.6	90
216S	1020	0.2	20	0	0	1000	188	*	*	8.1	86
026S	760	0.2	11	0	0	1000	104	*	*	3.0	30
026S	760	0.2	11	0	0	1000	104	*	2.08	*	*
027S	760	0.2	11	0	0	1000	104	*	5.10	*	*
030S	760	0.2	11	0	0	1000	104	*	7.00	*	*
031S	760	0.2	11	0	0	1000	104	*	2.10	*	*
032S	760	0.2	11	0	0	1000	104	*	2.63	*	*
033S	760	0.2	11	0	0	1450	104	*	6.67	6.67	61
034S	760	0.2	11	0	0	1450	104	*	6.23	6.23	84
035S	760	0.2	11	0	0	1450	104	*	7.27	7.27	96
101S	760	0.2	11	0	0	1000	104	*	1.50	3.75	*
103S	760	0.2	11	0	0	1000	104	*	9.00	10.00	76
622S	860	0.35	66	0	0	735	356	1055	6.76	*	90
623S	860	0.35	110	0	0	735	593	1025	8.30	*	100
624S	860	0.35	40	0	0	735	216	1200	9.55	*	100
625S	760	0.2	11	0	0	700	104	1030	2.27	*	92
626S	760	0.2	13	0	0	0	122	1060	6.38	*	92

* Not Mentioned
† Dilution
†† Annular and Window

Appendix I (cont.)

			Run Conditions						Wt. Collected		
Lot #	Laser Intensity (W/cm²)	Cell Pressure (atm)	SiH₄ (cm³/min)	NH₃ (cm³/min)	Ar † (cm³/min)	Ar †† (cm³/min)	Max. Gas Velocity at Nozzle (cm/sec)	Reaction Zone Temp. by Pyrometer (°C)	Filter (g)	Total in cell +Filter (g)	Total Eff. (%)
627S	760	0.2	7.5	0	0	700	71	850	2.27	*	90
628S	760	0.2	8.8	0	0	700	83	955	5.01	*	100
629S	760	0.2	5.5	0	0	700	52	790	0.99	>1.53	>85
630S	760	0.2	104	0	0	700	981	950	7.71	*	98
631S	760	0.2	38	0	0	700	358	1050	6.26	*	87
632S	760	0.2	38	0	0	700	358	1055	6.86	*	88
633S	760	0.2	60	0	0	700	566	980	7.72	*	90
634S	760	0.2	6.5	0	31.5	700	358	750	2.20	*	80
635S	760	0.35	66	0	0	735	356	*	7.90	*	89
636S	866	0.35	16	0	0	735	86	1215	2.34	*	86
637S	760	0.2	12.7	0	25.3	700	358	830	1.68	*	81
638S	380	0.35	66	0	0	735	356	930	4.92	*	98
024SN	2 x 10⁴	0.8	8	80	0	1000	207	*	*	small	*
025SN	2 x 10⁴	0.9	5.4	54	0	1000	124	*	*	8.0	~100
0400SN	760	0.75	11	110	0	1000	304	*	4.77	*	86
0401SN	760	0.75	11	110	0	1000	304	*	6.82	*	89
0402SN	760	0.75	11	110	0	1000	304	*	6.85	*	71

* Not Mentioned
† Dilution
†† Annular and Window

		Analysis		Excess	BET		TEM	Crystallite
Lot Number	Si	N	O	Si (%)	(m²/g)	(Å)	Diameter (Å)	Size (Å)
		(wt %)						
215S	–	–	*	–	60	429	*	*
216S	–	–	0.36	–	28.5	903	*	*
026S	–	–	0.17	–	83.0	310	*	*
027S	–	–	0.22	–	67	380	*	*
030S	–	see 01S		–	78	330	*	*
031S	–	see 01S		–	70	370	*	*
032S	–	see 01S		–	68	380	*	*
033S	–		*	–	110	230	*	*
034S	–	see 01S		–	79	325	*	*
035S	–	see 01S		–	94	270	*	*
101S	–		0.14	–	46.5	550	*	*
102S	–		0.14	–	*	*	*	*
103S	–		0.11	–	68	380	*	*
01S	(030S+031S+ 032S+034S+ 035S)		0.67	–	81	320	*	*
622S	–	–	<0.064	–	25	1046	*	306
623S	–	–	*	–	46	567	*	175
624S	–	–	*	–	22	1160	*	344

Powder Characteristics

* Not Measured

Appendix II (cont.)

Powder Characteristics

Lot Number	Analysis (wt %)			Excess Si (%)	BET		TEM Diameter (Å)	Crystallite Size (Å)
	Si	N	O		(m^2/g)	(Å)		
625S	-	-	0.28	-	39	650	*	172
626S	-	-	*	-	39	650	*	214
627S	-	-	*	-	64	401	*	118
628S	-	-	*	-	52	495	*	145
629S	-	-	*	-	70	366	*	84
630S	-	-	*	-	61	419	356	131
631S	-	-	0.70	-	42.5	604	525	175
632S	-	-	0.67	-	40.7	632	*	178
633S	-	-	*	-	48.5	530	*	149
634S	-	-	*	-	87.6	294	275	Amorphous
635S	-	-	*	-	31.3	823	*	250
636S	-	-	*	-	27.7	931	*	263
637S	-	-	*	-	71.5	360	*	Amorphous
638S	-	-	*	-	68.1	378	*	Amorphous
024SN	*	*	*	*	*	*	*	*
025SN	*	*	1.18	13	58.5	332	*	*
0400SN	*	*	*	*	80.1	250	*	*
0401SN	59.7	30.94	*	13	84.5	237	*	*
0402SN	62.4	30.5	.34	17	92.1	217	*	*

* Not Measured

REFERENCES

1. Bowen, H.K., October 1980, <u>Physics and Chemistry of Packing Fine Ceramic Powders</u>, under Contract DE-AC02-80ER10588, M.I.T., Cambridge, MA.

2. Haggerty, J.S. , and Cannon, W.R., October 1978, <u>Sinterable Powders from Laser Driven Reactions,</u> under Contract N00014-77-C0581, M.I.T., Cambridge, MA.

3. Haggerty, J.S., and Cannon, W.R., July 1979, <u>Sinterable Powders from Laser Driven Reactions</u>, under Contract N00014-77-C0581, M.I.T., Cambridge, MA.

4. Suyama, Y., and Kato, A., "TiO_2 Produced by Vapor Phase Oxygenolysis of $TiCl_4$", J. Am. Ceram. Soc., 59, 146-9 (1976).

5. Van de Hulst, H.C., <u>Light Scattering by Small Particles</u>, John Wiley and Sons, Inc., N.Y., 1957, Chptr.14.

6. Mitchell, A.C.G., and Zemansky, M.W., <u>Resonance Radiation and Excited Atoms</u>, Cambridge Univ. Press, Cambridge, 1961, p.163.

7. Johns, J.W.C., and Kreiner, W.A., "Measurement and Analysis of the ν_4 Band of Silane", J. Mol. Spectrosc. 60, 400-11 (1976).

8. Rutgers, G.A.W. and De Vos, J.C., "Relation between Brightness, Temperature, True Temperature and Colour Temperature of Tungsten", Physica, XX, 715-20 (1954).

9. Kuhl, Ch., Schlotterer, H. and Schwidefsky, F., "Optical Investigation of Different Silicon Films", J. Electrochem. Soc., 121, 1496-1500 (1974).

10. Friedlander, S.K., <u>Smoke, Dust, and Haze</u>, John Wiley and Sons, Inc., N.Y., 1977, Chptr.7.

11. Tikhomirov, M.V., Tunitzky, N.N. and Petrjanov, J.B., "On the Influence of van der Waals Forces on Coagulation of Aerosols", Acta Physicochimica, U.R.S.S., 17, 185-96 (1942).

12. Mason, S.G., "Orthokinetic Phenomena in Disperse Systems", J. Colloid Interface Sci., 58, 275-85 (1977).

13. Eastering, K.E., and Tholén, A.R., "Surface Energy and Adhesion at Metal Contacts", Acta Metall., 20, 1001-8 (1972).

14. Kingery, W.D., Bowen, H.K. and Uhlmann, D.R., <u>Introduction to Ceramics</u>, John Wiley and Sons, Inc., N.Y., 1976, Chaptr.5.

15. Braker, W. and Mossman, A.L., <u>Matheson Gas Data Book</u>, 5th Ed., Matheson Gas Products, E. Rutherford, N.J., 1971.

16. Weiser, H.B., "Inorganic Colloid Chemistry", in The Colloidal Elements, Vol. 1, John Wiley and Sons, N.Y., 1933, pp. 14-16, 163.

17. Wegelin, G., "Ueber die Herstellung, kolloider Losungen durch mecanische Zertielung", Kolloid-Z., 14, 65-9, (1914).

18. Astfalk, R. and Gutbier, A., "Ueber kolloides Silizium. Ein Beitrag zur Kenntnis der mechanisch-chemischen Dispersionmethoden", Kolloid-Z., 15, 23-7 (1914).

19. Williams, R., and Goodman, A.M., "Wetting of Thin Layers of SiO_2 by Water", Appl. Phys. Lett., 25, 531-2 (1974).

20. Peterlin, A., "Determination of Molecular Dimension from Light Scattering Data", Progress in Biophysics, 9, 175-237 (1959).

21. Kerker, M., The Scattering of Light and Other Electromagnetic Radiation, Academic Press, N.Y., 1969, Chap. 1.

22. Okamoto, S., and Hachisu S., "Ordered Structure in Monodisperse Gold Sol", J. Colloid Interface Sci., 62, 172-81 (1977).

23. Iler, R.K., "Formation of Precious Opal", Nature, 207, 472-3 (1965).

24. Greskovich, G., and Rosolowski, J.H., "Sintering of Covalent Solids", J. Am. Ceram. Soc., 59, 336-43 (1976).

25. Atkinson, A., Moulson, A.J., and Roberts, E.W., "Nitridation of High-Purity Silicon", J. Am. Ceram. Soc., 59, 285-88 (1976).

26. Longland, P., and Moulson, A.J., "The Growth of α- and β-Si_3N_4 Accompanying the Nitriding of Silicon Powder Compacts", J. Mater. Sci., 13, 2279-80 (1978).

27. Jennings, H.M., and Richman, M.H., "Structure, Formation Mechanisms and Kinetics of Reaction-Bonded Silicon Nitride", J. Mater. Sci., 11, 2087-98 (1976).

28. Messier, D.R., Wong, P., and Ingram, A.E., "Effect of Oxygen Impurities on the Nitridation of High-Purity Silicon", J. Am. Ceram. Soc., 56, 171-2 (1973).

29. Campos-Loritz, D. and Riley, F.L., "The Effect of Silica on the Nitridation of Silicon", J. Mater. Sci., 11, 195-8 (1976).

30. Moulson, A.J., "Reaction-Bonded Silicon Nitride: Its Formation and Properties", J. Mater. Sci., 14, 1017-51 (1979).

31. Grün, R., "The Growth of β-Si_3N_4 Single Crystals", J. Cryst. Growth, 46, 143-50 (1979).

32. Evans, A.G. and Davidge, R.W., "The Strength and Oxidation of Reaction Sintered Silicon Nitride", J. Mater. Sci., 5, 314-25 (1970).

33. Mendelson, M.I., "On Si Nitriding Kinetics and Mechanisms", J. Mater. Sci., $\underline{14}$, 1752-4 (1979).

34. Messier, D.R. and Wong, P., "Kinetics of Nitridation of Si Powder Compacts", J. Am. Ceram. Soc., $\underline{56}$, 480-5 (1973).

35. Evans, U.R., Corrosion and Oxidation of Metals, Edward Arnold Ltd., London, 1960, Chptr.20.

36. Kramer, T.M., "Nitriding of Silicon Formed by Laser Driven Decomposition of Silane", (B. S. Thesis, M.I.T., 1980).

37. Bird, Stewart and Lightfoot, Transport Phenomena, John Wiley and Sons, 1960, Chptr.9.

38. Danforth, S.C., "Effective Control of the Microstructure of Reaction Bonded Silicon Nitride (Si_3N_4) as Related to Improved Mechanical Properties", (Ph.D. Thesis, Brown University, 1978), Chptr.9.

39. Hausner, H., "Pressureless Sintering of Non-oxide Ceramics" in Energy and Ceramics, Materials Science Monograph, $\underline{6}$, 588-95 1980.

40. Ikegami, T., Tsutsumi, M., Matsuda, S., Shirasaki, S., Suzuki, H., "A Model Of Glass Densification with Simultaneous Grain Growth", J. Appl. Phys. $\underline{49}$, 4238-41 (1978)

41. Thummler, F., "Sintering and High Temperature Properties of Si_3N_4 and SiC" in Sintering Processes, Proceedings of the Fifth International Conference on Sintering and Related Phenomena, Materials Science Research, $\underline{13}$, 247-60 (1980).

42. Greskovich, C., and O'Clair, C., "Effect of Impurities on Sintering Si_3N_4 Containing MgO or Y_2O_3 Additives", Ceramic Bulletin, $\underline{57}$, 155-6 (1978)

43. Mitomo, M., "Pressure Sintering of Si_3N_4", J. Mater. Sci., $\underline{11}$, 1103-7 (1976)

44. Morgan, P.E.D., "Production and Formation of Si_3N_4 from Percusor Materials", Report # A-X3316, March - December 1973, pp.9-13.

45. Mazdiyasni, K.S., and Cooke, C.M., "Synthesis, Characterization, and Consolidation of Si_3N_4 Obtained from Ammonolysis of $SiCl_4$", J. Am. Ceram. Soc., $\underline{56}$, 628-33 (1973)